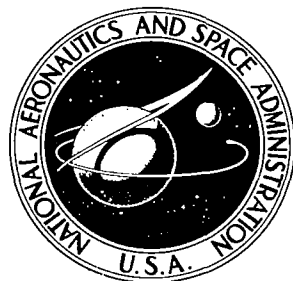


**NASA CONTRACTOR
REPORT**



NASA CR-1390

LOAN COPY: RETURN TO
AFWL (WL-2)
KIRTLAND AFB, N MEX

0060478



NASA CR-1390

RADIANT ENERGY TRANSFER MEASUREMENTS IN AIR

by Allen D. Wood and Kenneth H. Wilson

Prepared by

LOCKHEED AIRCRAFT CORPORATION

Palo Alto, Calif.

for Ames Research Center

NATIONAL AERONAUTICS AND SPACE ADMINISTRATION • WASHINGTON, D. C. • OCTOBER 1969

NASA CR-1390

TECH LIBRARY KAFB, NM



0060478

RADIANT ENERGY TRANSFER

MEASUREMENTS IN AIR

By Allen D. Wood and Kenneth H. Wilson

Distribution of this report is provided in the interest of information exchange. Responsibility for the contents resides in the author or organization that prepared it.

Issued by Originator as Report No. LMSC-681796

Prepared under Contract No. NAS 7-579 by
LOCKHEED AIRCRAFT CORPORATION
Palo Alto, Calif.

for Ames Research Center

NATIONAL AERONAUTICS AND SPACE ADMINISTRATION

For sale by the Clearinghouse for Federal Scientific and Technical Information
Springfield, Virginia 22151 - Price \$3.00

ABSTRACT

Plasma temperatures and total radiant intensities were measured in air plasmas created in the reflected shock region of a 12-inch diameter, arc-driven shock tube. The temperatures were required to explore the difference between the total intensity measurements and theoretical predictions which were evaluated at the gasdynamic property values. The temperature measurements utilized the following spectroscopic techniques: (1) measuring the integrated intensity of certain atomic lines and multiplets, (2) fitting profiles to measured line shapes, and (3) measuring the spectral intensity of the continuum at 4935 Å. Temperatures between 10,750-13,000 K were measured with a typical precision of $\pm 4\%$. This precision could not be maintained at higher temperatures. The results indicate that, on the average, the measured temperatures were 4% below the gasdynamic values which could account for the difference between the total intensity measurements and the predictions in this temperature range. Further, the erratic shot to shot deviations of 0 to 8% between the measured and gasdynamic temperatures suggests that the actual plasma temperatures were not adequately predictable from the incident shock velocity.

ACKNOWLEDGEMENTS

The authors acknowledge the assistance of Dr. Peter R. Forman, now with the Los Alamos Scientific Laboratory, who was instrumental in guiding the initial spectroscopic efforts during the summer of 1967, and that of Dr. William S. Cooper III of the University of California-Lawrence Radiation Laboratory for his helpful consultations. The authors also thank Miss Helen R. Kirch for her able programming assistance and, last but not least, Jack C. Andrews and Eugene R. Grozenski for their capable operation of the shock tube.

CONTENTS

	Page
INTRODUCTION	1
DESCRIPTION OF APPARATUS AND TECHNIQUE	3
Homochromatic Photometry	3
Instrument Function	8
Spectrograph Optical System and Rapid-Closing Shutter	12
Spectrograph Film and Exposure	16
Polychromator	19
Polychromator Calibration and Analysis	23
Combination of Results from Spectrograph and Polychromator	27
PLASMA THERMOMETRY	28
General Error Analysis	28
Derivatives of Plasma Properties	29
Radiant Energy Transport Equations	30
Thermometry of Line Intensity Measurements	32
Error Analysis for Line Intensity Thermometry	34
Thermometry of Line-Shape Fitting	37
Error Analysis of Line-Shape Thermometry	30
SPECTRAL SURVEYS	42
Spectral Identification	42
Proof of Steady State	48
Selection of Plasma Thermometers	51
RESULTS	53
Examples of Shape-Fitting	53
Example of Line Overlap	60
Examples of Combined Results	61
The Thermometric Use of the Continuum	67
Results of the Plasma Temperature Measurements	68
CONCLUSIONS AND RECOMMENDATIONS	73
APPENDIX	76
REFERENCES	81

LIST OF FIGURES

Fig. 1	Results of Instrument Function Measurement at Three Wavelengths	10
Fig. 2	Optical System for Spectrograph	13
Fig. 3	Rapid-Closing Shutter	15
Fig. 4	Spectral Sensitivity of Various Kodak Films	18
Fig. 5	Optical System for Polychromator	21
Fig. 6	Partial Derivatives of Plasma Properties Evaluated Along the Reflected Shock Hugoniot	31
Fig. 7	Microdensitometer Traces of Representative Spectrograms	43
Fig. 8	Photomultiplier Traces from Polychromator on Shot #590 ($U_S = 6.85 \text{ mm}/\mu\text{sec}$)	49
Fig. 9	Various Photoelectric Traces from Twelve Shots	50
Fig. 10	Example of Shape-Fitting Process for $H\alpha$ on Shot #601 ($U_S = 7.00 \text{ mm}/\mu\text{sec}$)	54
Fig. 11	Example of Shape-Fitting Process for NI^9 on Shot #601 ($U_S = 7.36 \text{ mm}/\mu\text{sec}$)	55
Fig. 12	Example of Shape-Fitting Process for NI^9 on Shot #605 ($U_S = 7.36 \text{ mm}/\mu\text{sec}$)	57
Fig. 13	Example of Shape-Fitting Process for NI^9 on Shot #606 ($U_S = 7.99 \text{ mm}/\mu\text{sec}$)	58
Fig. 14	Results of Fitting a Shape to $H\beta$ Profile on Shot #603 ($U_S = 6.95 \text{ mm}/\mu\text{sec}$)	59
Fig. 15	Profile Extremes About NI^{21}	62
Fig. 16	Combined Results for Shot #603 ($U_S = 6.95 \text{ mm}/\mu\text{sec}$)	63
Fig. 17	Combined Results for Shot #605 ($U_S = 7.36 \text{ mm}/\mu\text{sec}$)	64
Fig. 18	Combined Results for Shot #606 ($U_S = 7.99 \text{ mm}/\mu\text{sec}$)	65
Fig. 19	Results of Temperature Measurements	69
Fig. 20	Comparison of the Results from the Various Thermometric Techniques	71
Fig. A1	Experimental Results and Theoretical Prediction for the Total Radiant Intensity	77
Fig. A2	Experimental Results and Theoretical Prediction for the Radiant Intensity Transmitted by a Quartz Window	78

LIST OF TABLES

Table 1	Listing and Identification of Prominent Air Multiplets	45
Table A1	Radiant Intensity Prediction at Conditions in the Reflected Shock Region	79
Table A2	Calculated Thermodynamic States of the Reflected Shock Region	80

FOREWORD

This final report covers the work performed for the National Aeronautics and Space Administration Headquarters, under the terms and specifications of Contract NAS 7-579, issued through the NASA Pasadena Office, 4800 Oak Grove Drive, Pasadena, California 91103. The Technical Monitor on this contract was Mr. William A. Page, Hypersonic Free Flight Branch, NASA-Ames Research Center, Moffett Field, California 94035.

The work was performed in the Aerospace Sciences Laboratory, R. Capiaux, Manager, of the Lockheed Palo Alto Research Laboratory.

FINAL REPORT
Contract NAS 7-579
RADIANT ENERGY TRANSFER MEASUREMENTS IN AIR

INTRODUCTION

The work done under this contract can be split into two distinct areas: one involves measurements and theoretical predictions of the spectrally-integrated radiant intensity of high-temperature air while the other concerns spectral measurements obtained using various spectroscopic techniques. Because the latest results of the spectrally-integrated area have already been published,¹ this effort is briefly summarized below. The results and conclusions obtained serve as the introduction to the spectroscopic effort which occupies the bulk of this report.

The measurements in both areas were performed in the reflected shock region of a 12-in. diam. shock tube equipped with an arc-heated driver. The test gas was air at $P_1 = 0.2$ torr; the incident shock speeds were 6.5-9.5 mm/ μ sec and yielded reflected shock plasmas of 10-16,000 K, 2-5 atm, and $\rho/\rho_0 \approx 0.033$ Amagats.

The spectrally-integrated effort involved measurements of the radiant intensity from these plasmas at paths of 3-12 cm using energy detectors in both a windowless and a window-type configuration. The salient results are shown in the two figures located in the appendix of this report. These show a comparison between the experimental results and theoretical predictions for both the total (i.e. windowless) radiant intensity (Fig. A-1) and for that fraction transmitted by a quartz window (Fig. A-2). Also included in the appendix are tables containing numerical values for the radiant intensity predictions (Table A-1) and the reflected shock Hugoniot states (Table A-2) on which the figures were based. A more complete description of the experimental apparatus and technique and the origin of the theoretical predictions is given in Ref. 1.

The comparisons between experiment and theory as presented by Figs. A-1 and A-2 show essentially the same behavior: good agreement at the lowest incident shock velocities with the experimental data falling steadily below the predictions and reaching a factor of two below at the highest velocity. It is important to appreciate that the experiment measured the radiant intensity as a function of incident shock velocity while the predictions were evaluated at the thermodynamic states obtained from gasdynamic considerations. Therefore these comparisons between theory and experiment must include a consideration of the validity of the gasdynamic temperature.

This basic question, which precluded a meaningful comparison between theory and experiment, motivated the spectroscopic effort which, in fact, occupied the bulk of the past contractual period. This work had two important objectives. The first was to measure the plasma temperature directly and hence resolve the fundamental difficulty discussed above. The second was to generate spectral information about high-temperature air radiation to permit a more discerning evaluation of current radiation theories. The effort was concentrated on the former and more important objective. For reasons to be discussed later, the plasma temperatures were only measured to 13,500 K. However even these measurements revealed significant deviations between the actual and the gasdynamic plasma temperature and further work in the area is continuing.

The temperature measurement problem can be placed in perspective by noting that the total intensity for a 5 cm path can be represented by $I \propto P^{0.9} T^X$ over the conditions of interest. The temperature exponent is about 12 at 10,000, 9 at 13,000 and 5.5 at 16,000 K. Thus a 30% change in radiant intensity corresponds to a 2% change in temperature at 10,000 K and a 5% change at 16,000 K. Thus it is clear that precise temperature measurements were required.

This high sensitivity of radiation to temperature, which requires precise temperature measurements, can be used to advantage by determining a temperature through measurements of radiative quantities. Two that proved suitable were the absolute intensities of certain well-known atomic lines and the shapes

(i.e. the half-widths) of these and other lines. As discussed later, a line intensity measurement yields a temperature based on a Boltzmann distribution of the upper state population while a shape measurement yields the electron density which is related to temperature through the Saha equation.

The measurement of these two quantities required quite different instrumentation and techniques. The line shapes were determined by photometric techniques via time-integrated spectrograms taken using film and a rapid-closing shutter in a spectrograph. Photographic recording captures a wealth of information about relative spectral intensities which is essential for determining line shapes, however it is not amenable to measuring absolute spectral intensities. These were measured over narrow spectral intervals using photoelectric recording techniques in a polychromator (i.e. a multi-channel monochromator) and were, of course, time-resolved measurements. The features of these two spectroscopic techniques are summarized below:

<u>Instrument</u>	<u>Recording Technique</u>	<u>Time Variation</u>	<u>Type of Measurement</u>	<u>Spectral Variation</u>
Spectrograph	Photographic	Time-integrated	Relative	Spectral
Polychromator	Photoelectric	Time-resolved	Absolute	Spectrally- integrated

As noted, the techniques complement each other and the combined results can yield a fairly complete picture of the plasma radiation. In fact, as will be explained later, the results of both techniques were required to obtain temperatures from both line intensity and line shape measurements.

DESCRIPTION OF APPARATUS AND TECHNIQUE

Both types of spectroscopic measurements were made on the same kind of instrument: Model 78-000 Jarrell-Ash 1.5 meter Wadsworth spectrographs. Each contained a 590 groove/mm grating and could cover from 2100 to 7800 Å at one time in first-order with a reciprocal linear dispersion of about 11.2 Å/mm. The ruled grating areas were 54 x 40 mm which means that the instruments were effectively f/29 and had a theoretical resolution of 0.07 Å at 2200 Å and 0.24

A at 7800 Å. These parameters would dictate a spectroscopically-optimum entrance slit width of about 17 μ for recording at 6,000 Å. In practice resolution was sacrificed to gain light and 50 μ entrance slits were used. Since these 50 μ entrance slits were from 2 to 8 times wider than the width for optimal resolution, diffraction effects were small and the resolution was very near the spectral width of the entrance slit (0.55 Å) as will be discussed shortly. One of these instruments was used as a conventional spectrograph while the other was modified for use as a polychromator. The spectroscopic techniques involved in these two different usages will be discussed separately.

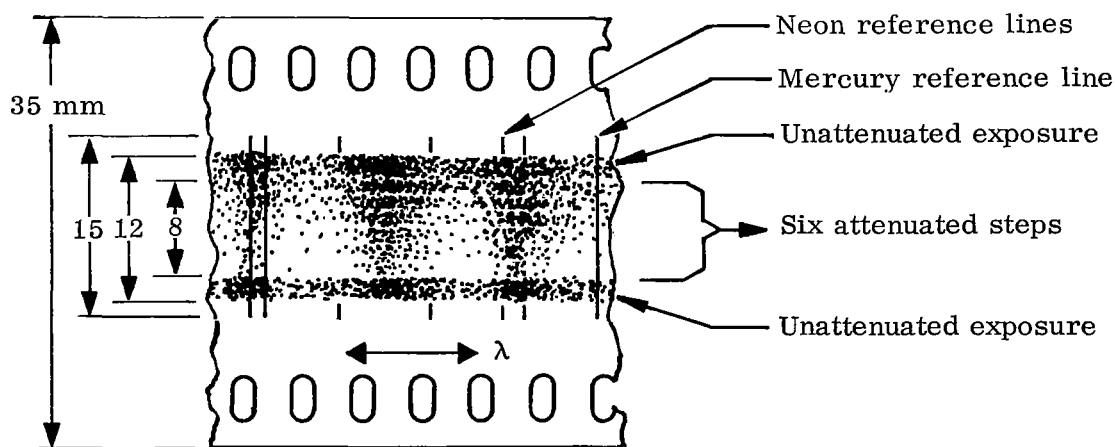
The terminology is however the same and begins with the spectral intensity (i.e. $I_\lambda(\lambda)$ in $\text{W}/\text{cm}^2\text{-sr-}\mu$) emitted by the plasma. Some of this radiation is collected by the spectrograph, dispersed, and brought to a spectral focus along the focal plane. Here it is characterized by the focal plane heat flux (i.e. $q(\lambda)$ in W/cm^2) which varies with distance along the focal plane or, more conveniently, as wavelength. The role of an exit slit will be discussed later. A film placed here receives this heat flux over an exposure time with the result that a certain energy per unit area is deposited on the film. By the photographic development process, this energy per unit area is converted into an optical density which, by photometric techniques, is converted back into a spectral exposure (i.e. $e(\lambda)$ in erg/cm^2) or a relative spectral exposure [$e(\lambda)/e(\lambda_0)$]. At this point a distinction is made between relative spectral exposure and intensity. These are related through the instrument function which will be discussed later. First the methods by which the relative exposure was obtained from an exposed film will be discussed.

Homochromatic Photometry

The spectrograph was used to obtain relative spectral exposures by the technique of homochromatic photometry (ref. Chap. 10 of Sawyer² or Chap. 7 of Harrison et al.³). This technique essentially assumes that the wavelength intervals under consideration are sufficiently narrow that film sensitivity variations with wavelength are negligible. Otherwise, conventional photometric techniques are employed.

A photographic emulsion, upon being exposed and developed, contains particles of silver which make the negative appear dark or even black when viewed by transmitted light. This darkness is characterized by an optical density which is the logarithm of the reciprocal transmittance. The relation between optical density and the amount of exposure is expressed as a density-log exposure curve commonly known as an H-D curve. Since optical densities are measured after the fact, an H-D curve can only be obtained if the negative contains areas of known exposure and, for relative work, these exposures need only be known relative to one another. The whole technique of homochromatic photometry involves obtaining and using the appropriate H-D curves. However, this is not trivial because the H-D curves depend on a great many parameters including the wavelength and the rate, amount, and time of exposure, the age, history and of course type of film, and the many variables (time, temperature, type, concentration, etc.) of the development process. Good technique requires that the H-D curves be obtained under conditions as close as possible to those of the actual experiment.

Because the Wadsworth mount is stigmatic, this was readily accomplished by placing a calibrated neutral density step wedge directly in front of the entrance slit during the exposure to the plasma radiation. The resultant bands of reduced exposure are shown by the following sketch of a typical negative.



Sketch of a typical spectrogram showing the various exposure bands and the reference wavelength lines.

The step wedge was mounted on a special plate which replaced the Hartmann diaphragm typically found on most spectrographs. The step wedge had six, metal-film attenuator steps on a quartz substrate. The steps had optical density differences of about 0.2 and occupied 8 mm of a 15 mm tall entrance slit. These dimensions are reflected in the above sketch because the spectrograph had unity magnification.

This sketch also indicates how the entire 15 mm image distance was utilized to record an unattenuated exposure and reference wavelength information. The technique was to remove the dark slide from the spectrograph camera shortly before each shot. Then a mercury spectrum was put over the entire height of the entrance slit followed by a neon spectrum over the extreme edges. These spectra were obtained from low-pressure discharge tubes and the exposure times were several seconds. The purpose of the neon spectrum was to provide additional lines in the interesting red region where very few first-order mercury lines exist. Then the step wedge was inserted, the shock tube fired, and finally the dark slide was replaced and the film removed and developed.

By this technique, each spectrogram contained all the wavelength information needed to obtain the dispersion and absolute wavelengths and all the exposure information to obtain the H-D curve of the film at any desired wavelength and hence the relative exposure profile. This latter process involved several steps which are outlined below.

As shown above, the six steps of the step wedge produced bands of reduced exposure across the film. The amount of reduction in each band depended on the optical density of each step and determining quantitative values can lead to much confusion. Optical density is defined by the logarithm of I_0/I where I_0 is the amount of light incident and I the amount transmitted. The confusion lies in how the transmitted light is collected. Since some filters mainly scatter light (photographic emulsion), some absorb (gelatin), while others mainly reflect (metal film), the solid angle used to collect the transmitted light is important. Thus optical densities are further

qualified by the adjectives specular or diffuse. The correct density for the present application was that obtained by collecting the light transmitted into an $f/29$ solid angle - the same as the spectrograph.

To accomplish this, the spectrograph entrance slit (with the step wedge in place) was illuminated by a tungsten strip lamp. A small slit was placed on the envelope of a photomultiplier tube and the slit-tube assembly was carefully located in the focal plane at various wavelengths. Then this assembly was racked up and down (ref. above sketch) across the various bands. The ratio of the outputs gave the transmittance of each step: they were 0.63, 0.40, 0.27, 0.17, 0.115, and 0.077 and were uniform from 4500-7000 Å.

The optical densities of each spectrogram were measured using a Jarrell-Ash Model JA 2310 Microdensitometer equipped with a strip chart recorder. The microdensitometer output and hence the pen deflection was linearly proportional to the transmittance T of the emulsion which is related to density by $D = 2 - \log_{10}(T)$ with T in percent. By using special density paper (Bristol Chart No. R0333) in the recorder, the algebraic conversion step was eliminated and density was read directly (albeit nonlinearly) from the paper. The microdensitometer slit was typically set at 0.7 mm tall to avoid the edges of the exposure steps. Since the Wadsworth mount is only truly stigmatic at the grating normal (5100 Å), the edges became obscure at wavelengths far from the grating normal. The width was a compromise value of 25 μ or roughly half the physical slit width of the spectrograph. A wider microdensitometer slit would integrate across more film grains and hence reduce noise, but this would also widen the instrument function which will be discussed shortly. The scanning rate was kept low (equivalent of 5.5 Å/min) to allow time for the recorder pen to follow all the spectral details.

H-D curves were constructed by measuring the optical densities of the various exposure bands at the wavelengths of spectral features of interest. The basic premise of homochromatic photometry is tantamount to assuming that each H-D curve applies over, say, the full width of the line or multiplet under consideration. Therefore, the microdensitometer scan along any exposure band

could be converted, through the H-D curve, to an ordinate of relative exposure. Normally the unattenuated exposure band was used for this procedure since the negatives were generally underexposed and it is desirable to work on the most linear portion of the H-D curve. The reference wavelengths included on the microdensitometer scans allowed the wavelength at any point to be determined by linear interpolation. In practice the wavelengths were often read directly from a preset Gerber scale. Thus the final result of this technique was a plot of relative exposure versus wavelength - a relative exposure profile. Examples are given later in this report.

Instrument Function

The relation between the exposure profile discussed above and the spectral intensity profile emitted by the plasma is described by the instrument function. The spectral features of the emergent intensity were broadened both in the spectrograph itself since at best the focal plane contains a series of overlapping monochromatic images of the entrance slit and in the microdensitometric scanning process where again another slit of finite width was employed.

Suppose that the entrance slit (area A_s) was uniformly irradiated by a steady intensity $I(\lambda^*)$ from a monochromatic source at wavelength λ^* . Assuming that the grating represents the limiting aperture, the spectrograph subtends a solid angle A/f^2 where A is the grating area and f is the slit-to-grating distance.[†] Thus the product $I(\lambda^*) A_s A/f^2$ represents the rate at which monochromatic energy enters the spectrograph and of this a fraction $\tau(\lambda^*)$ reaches the focal plane in first-order. This energy is distributed along the focal plane in a yet unknown manner, however the integral of the focal plane heat flux $q(\lambda)$ must equal the incoming rate, hence

$$I(\lambda^*) \tau(\lambda^*) \frac{A_s A}{f^2} = \frac{h}{RLD} \int_{\Delta\lambda} q(\lambda) d\lambda \quad (1)$$

[†]The presence of collimating lenses or mirrors complicates this definition but should not cause difficulty by noting that the expression represents the solid angle that the instrument subtends at the entrance slit.

where h is the height of the focal plane, RLD the reciprocal linear dispersion, and $\Delta\lambda$ the wavelength increment over which $q(\lambda)$ is nonzero. (It is convenient to express lengths along the focal plane in terms of wavelengths by the expression $d\lambda = RLD \, dx$).

Now if a spectrogram were taken of this monochromatic irradiation, the resultant relative exposure profile is defined to be the instrument function, $F(\lambda-\lambda^*) \equiv e(\lambda)/e(\lambda^*)$, where $e(\lambda)$ is the spectral exposure at wavelength λ and is normalized to the maximum value $e(\lambda^*)$. The instrument function for this experiment is shown by Fig. 1. It was measured at three wavelengths using the reference mercury and neon spectra along the edge of an actual shot spectrogram together with H-D curves obtained from nearby spectral features. The particular lines were selected because they were weak and the resultant film densities were comparable to that of the plasma spectrum. Bright reference lines could easily become grossly overexposed and lead to broadening by film halation. It is noted that the values at each of the three wavelengths are quite similar and hence the instrument function was not dependent on wavelength. Close scrutiny shows that the broadest function was obtained from the reddest line which should be expected since diffraction effects are least negligible at long wavelengths.

Since diffraction effects should be small because of the relatively wide entrance slit employed, the instrument function would be expected to resemble the result of scanning a geometric image of the $50 \, \mu$ entrance slit with a $25 \, \mu$ microdensitometer slit; i.e. a triangular function with a base of $100 \, \mu$ or $1.12 \, \text{\AA}$. Since the actual function was trapezoidal with a slightly narrower base, the actual microdensitometer slit was probably slightly smaller ($\sim 22 \, \mu$). More important is the elimination of other types of broadening phenomena such as improper focus, optical aberrations, etc. This predictability of the instrument function means that the monochromatic energy was uniformly distributed over the geometric image of the entrance slit in the focal plane. This will be important in the polychromator discussion which will follow shortly.

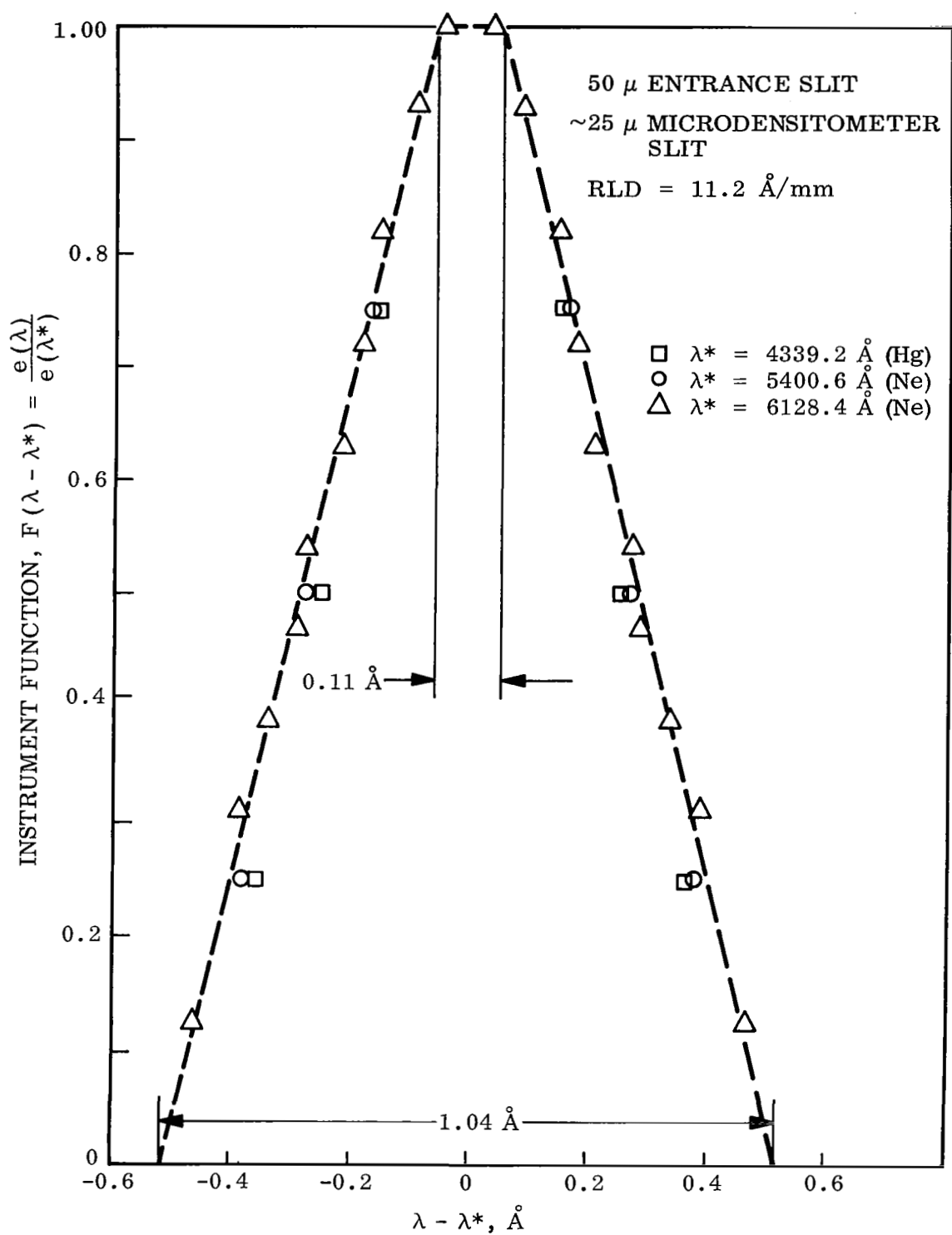


Fig. 1 Results of Instrument Function Measurement at Three Wavelengths

The equation relating the absolute exposure at a wavelength λ resulting from the steady monochromatic irradiation of the entrance slit at a wavelength λ^* is obtained from Eq. (1) by introducing an exposure time t and the definition of the instrument function with the result

$$e(\lambda) = \frac{W(RLD)A}{f^2} \tau(\lambda^*)t \frac{I(\lambda^*)F(\lambda-\lambda^*)}{\int_{\Delta\lambda} F(\lambda-\lambda^*)d\lambda} \quad (2)$$

For a stigmatic instrument with unity magnification, the factor A_s/h becomes W , the physical width of the entrance slit.

The extension of this concept to non-monochromatic intensities is straightforward. Any spectral intensity $I_\lambda(\lambda)$ can be broken into a series of "monochromatic" lines by multiplying by a differential wavelength increment $d\lambda$ and treating each incremental line in the above manner. The resultant exposure at any wavelength is the sum of all possible contributions and is given by

$$e(\lambda) = \frac{W(RLD)A}{f^2} \tau(\lambda)t \frac{\int I_\lambda(\lambda')F(\lambda-\lambda')d\lambda'}{\int_{\Delta\lambda} F(\lambda-\lambda')d\lambda'} \quad (3)$$

Here the transmittance $\tau(\lambda)$ was assumed to remain constant over the instrument function. This equation is generalized by invoking the well-known principle that the intensity of a source cannot be increased by optics. Thus the intensity in the above equation is that emitted by a source provided that (1) the transmittance includes that of the optical system and (2) the grating and the slit remain the limiting apertures.

The above equation relates the spectral intensity emergent from the plasma to the absolute spectral exposure. The techniques of homochromatic photometry yield relative spectral exposure profiles. These are expressed in terms of the instrument function by normalizing the above equation with respect to a peak exposure $e(\lambda_0)$. Since it was shown that the instrument function was independent of the absolute wavelength, Eq. (3) becomes:

$$\frac{e(\lambda)}{e(\lambda_o)} = \frac{\int_{\Delta\lambda} I_\lambda(\lambda') F(\lambda - \lambda') d\lambda'}{\int_{\Delta\lambda} I_\lambda(\lambda') F(\lambda_o - \lambda') d\lambda'} \quad (4)$$

If changes in the spectral intensity over the width of the instrument function are neglected, this equation reduces to

$$\frac{e(\lambda)}{e(\lambda_o)} \approx \frac{I_\lambda(\lambda)}{I_\lambda(\lambda_o)}$$

which is to say that the relative exposure profile is equal to the relative spectral intensity profile provided that the instrument function is negligibly narrow.

In the preceding discussion it was tacitly assumed that the plasma intensity remained constant throughout the exposure time. The constancy was verified on each shot by a photoelectric monitor of the zero-order light in the spectrograph and also by the simultaneous signals from the various polychromator channels. Examples of these traces will be presented later.

Spectrograph Optical System and Rapid-Closing Shutter

The spectrograph was coupled to the shock tube by the optical system shown in Fig. 2. This optical system was designed with two requirements in mind: first, the accepted beam had to be reasonably narrow over the full 30 cm diameter of the shock tube to avoid viewing the end wall and interface. Secondly, the entrance slit (or, more precisely, the step wedge) had to be uniformly irradiated so that the technique of homochromatic photometry would be valid. This latter requirement was met by using the 10 cm f.l. lens (ref. Fig. 2) to focus an image of the entrance slit on the 14 cm f.l. lens. Since this latter lens was uniformly irradiated by the reflected shock plasma, then so was the entrance slit. The accepted beam was made narrow by employing the cylindrical lens at slightly more than a focal length away from the 14 cm f.l. lens. The centerline of the beam was located 7 mm from the end wall.

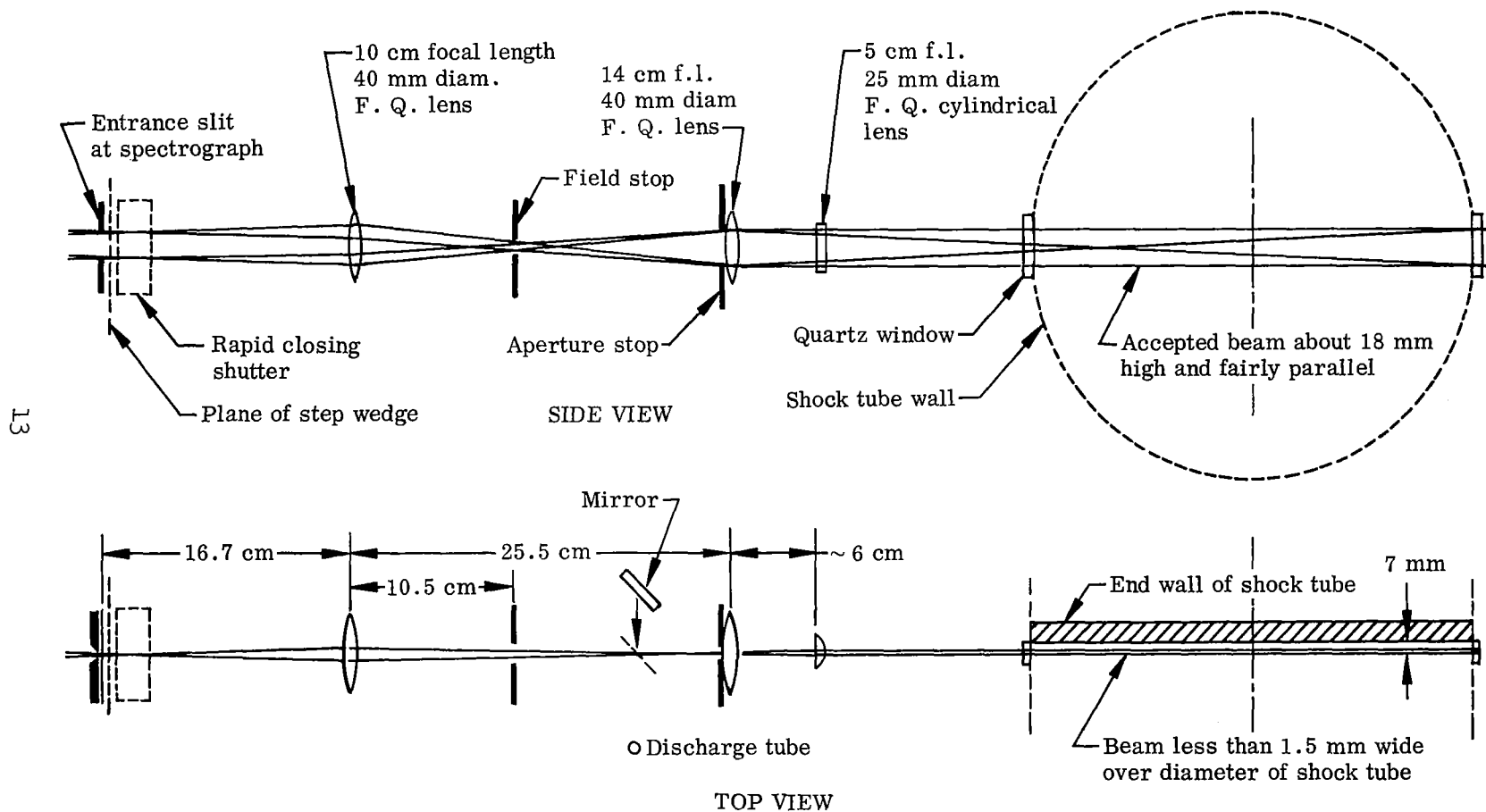
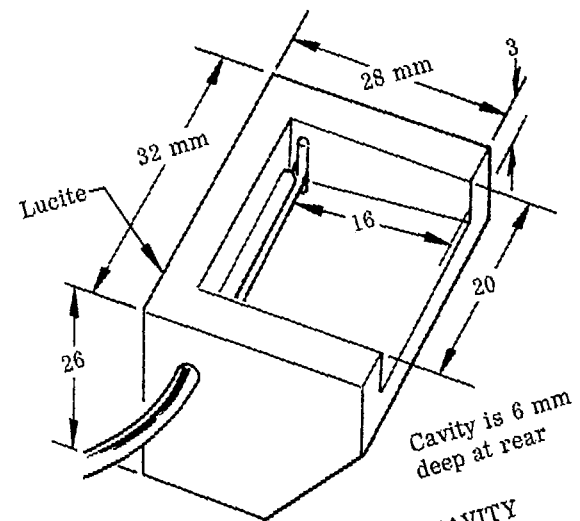
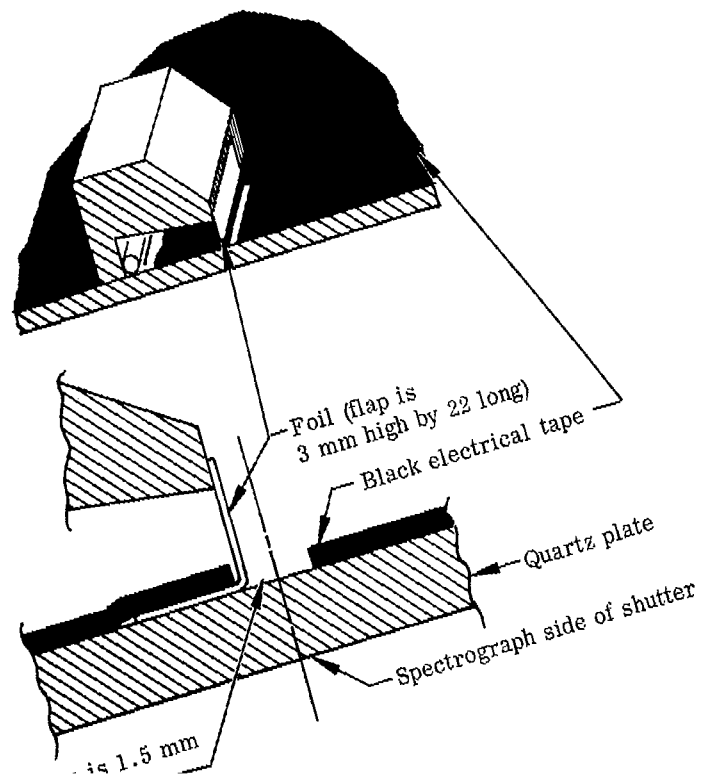


Fig. 2 Optical System for Spectrograph

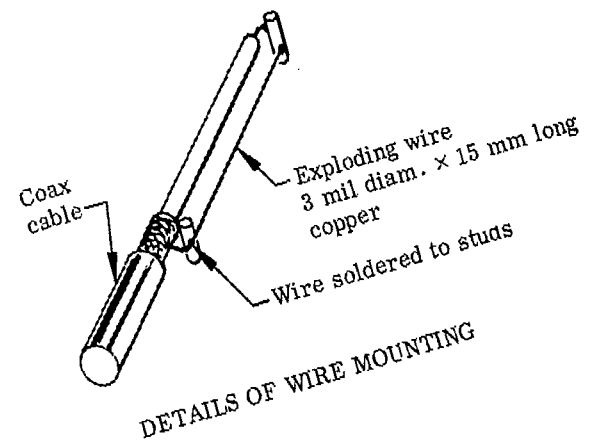
This optical system used ordinary fused quartz lenses throughout and transmitted down to at least 2500 Å (this was probably the film cut-off caused by gelatin absorption). It was not achromatic and hence was focused in the green (~ 5500 Å) as a compromise over the visible region. It did go out of focus in the ultraviolet but this was of little consequence since this region was used for survey purposes only. The field and aperture stops were placed at images of the grating and slit to prevent excess light from entering the spectrograph and causing possible scattered light problems. These stops were slightly larger than the size of the visible images so that they were not limiting apertures. The spectrograph was fully illuminated in the visible region by this optical system.

In practice the spectrograph was left open from several seconds prior to each shot until about 30 μ sec after the reflected shock passed through the field of view. The exposure from the ambient light and the incident shock was negligible in comparison to that from the reflected shock plasma. Thus the shuttering requirements were for a rapid-closing, capping-type shutter.

The concept of this shutter was obtained from the article by Wurster⁴ although the final design was somewhat different. Basically the shock wave and/or debris from an exploding wire are used to bend a flap of metal foil through 90° and hence cover an aperture. Figure 3 contains several sketches to show how the wire was mounted and how the effects of the explosion were directed toward the flap. The entire assembly shown was mounted in a brass case 75 mm diameter by 40 mm thick. The foil was ordinary "Super Strength Alcoa Wrap" which had a thickness of 0.7 mil. The 3 mil diameter by 15 mm long copper wire was exploded by switching a 4 μ fd capacitor charged to about 3.3 kV via a 5C22 thyatron tube. The shutter would typically close in 5 μ sec with closure occurring about 35 μ sec after a trigger pulse was sent to the thyatron grid. The initial firing of the thyatron caused an electromagnetic disturbance in the other instrumentation. Therefore the timing was such that the thyatron was triggered before the reflected shock reached the field of view of this instrumentation and hence this disturbance occurred and was over before any reflected shock information was recorded.



DETAILS OF WIRE CAVITY



DETAILS OF WIRE MOUNTING

The action of the shutter was recorded for each shot by the photoelectric monitor of the spectrograph zero-order light. Thus the exposure time and the temporal behavior of the radiation during the exposure were known. Examples of this monitor will be given later. No radiation emitted by the shutter was discernable on any spectrogram and this is probably explained by the physical location of the shutter components; the exploding wire is surrounded by the wire cavity until the flap opens and hence the shutter closes.

All the spectroscopic work was done with a first-order spectrum. The higher-order spectra were blocked by placing a strip of Rohm and Hass Type II UVA Plexiglas along the focal plane from 3800 Å to beyond 7000 Å. This material is opaque below 3365 Å and transmits well above 3460 Å. Thus the combination of quartz lenses and Plexiglas cleared the first-order spectrum to about 6800 Å. A Wratten #8 (K2) filter was used occasionally to clear to even longer wavelengths, but this appeared to cause interference problems when used near the focal plane and, since the film sensitivity dropped sharply above about 6900 Å, this filter was seldom used.

Spectrograph Film and Exposure

The film used throughout the experiment was Kodak 2475 Recording Film. This is an extremely high speed (ASA 1000) panchromatic film with extended red sensitivity. It was developed for 5 minutes in room-temperature DK-50 following the manufacturer's recommendation. Unfortunately high speed film is grainy and 2475 film is rated as a coarse-grained film. Attempts to use a slower, finer-grained film (Kodak 2496 RAR film) met with no success because of insufficient light.

Although the spectrograph was used to obtain relative rather than absolute exposures, inevitably one wishes to work on an approximately absolute basis if only to consider exposure details. The necessary equation is obtained from Eq. (3) by neglecting the effect of the instrument function with the result

$$e(\lambda) = \left[\frac{W(RLD)A}{f^2} \right] \tau(\lambda) I_{\lambda}(\lambda)t \quad (5)$$

For the JACO 1.5 m spectrograph with a 50 μ slit, the bracketed factor is 5.4×10^{-8} μ -sr ($A = 40 \times 54 \text{ mm}^2$, $W = 50 \mu$, $RLD = 11.2 \text{ A/mm}$, $f = 1.5 \text{ m}$).

The transmission of the spectrograph was obtained by illuminating the entrance slit with monochromatic light obtained from a monochromator through a system of lenses and apertures with a larger f/number (i.e. a smaller solid angle) than that of the spectrograph. Thus the ratio of the light reaching the focal plane to that measured behind the entrance slit gave the transmission (for first-order) of the spectrograph. This was measured with a linear photomultiplier tube and the result was that the transmission reached a maximum value of 60% at 3500 A and dropped steadily to about 30% at 7000 A. The transmission of the optical system was determined by back-lighting the spectrograph and determining the ratio of the light emergent from the last lens to that emerging from the entrance slit. This ratio was about 50% at all wavelengths. The product of these two numbers thus yields the transmission required in the above equation.

To measure the sensitivity of the Kodak 2475 Recording Film, a 0.16 sec exposure was taken of a calibrated tungsten strip lamp - a source of known intensity. The resultant spectrogram was densitometered at a number of wavelengths to obtain the H-D curves which, in this case, were used to yield the relative exposure necessary to obtain a density of 0.3 above fog. The absolute value of the 100% exposure was calculated from the above equation using the known lamp intensity and the measured transmission. The results are shown on Fig. 4 together with the Kodak curves for this and two other films. As can be seen, the data points agree quite well with the manufacturer's information and a log sensitivity of 2 is typical for 2475 film. Whether this value of film sensitivity is valid for a calculation of an intensity from the reflected shock plasma at a typical exposure time of 30 μ sec depends on the reciprocity behavior of the film. The reciprocity law states that the film

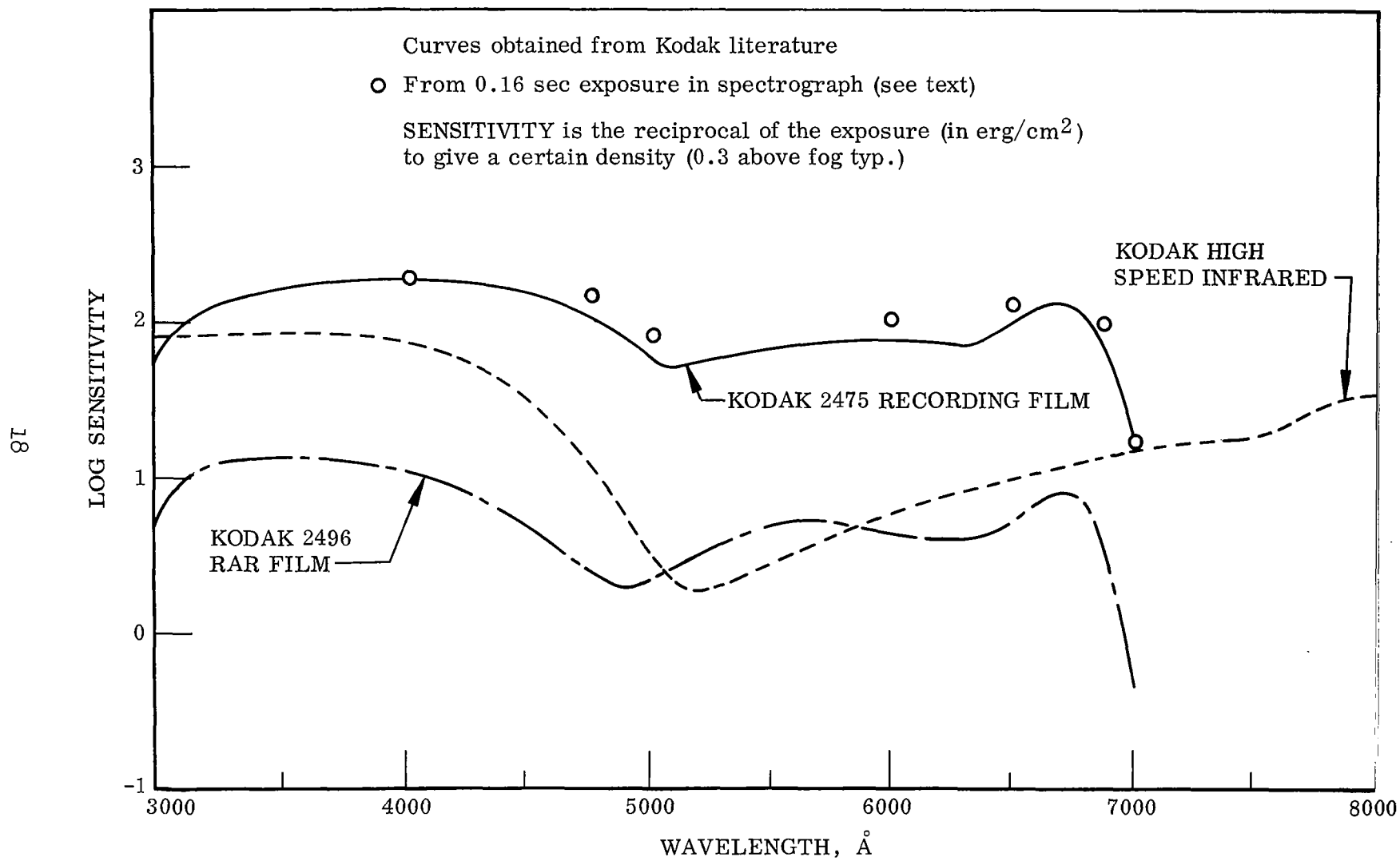


Fig. 4 Spectral Sensitivity of Various Kodak Films

sensitivity is dependent only on the product of the exposure rate and time and is independent of either factor taken separately. Milne and Eyer⁵ could find no reciprocity failure for Kodak Royal-X Pan Recording Film (a type similar to 2475) at exposures from 10^{-4} to 10^{-8} sec so the neglect of reciprocity failure for this calculation appears to be valid.*

Thus we assume that an exposure of 10^{-2} erg/cm² is required for a density of 0.3 above fog (a minimal exposure). Using the above equation and assuming a transmittance of 20%, the intensity required for a 30 μ sec exposure is $I = 3100$ W/cm²-sr- μ . For visible radiation and a 30 cm pathlength in the reflected shock plasmas of this experiment, this spectral intensity is typical of the radiation at line centers from an 11,000 K plasma and continuum radiation from plasmas above 12,500 K.

Thus it is clear that the experiment did not enjoy excess light and the finer-grained but less-sensitive (by factor of 10) Kodak 2496 Film could not be employed. Recently another extremely fast Kodak film has become available - Kodak 2485 High Speed Recording Film (formerly Type SO-166) - and promises to be nearly 10 times faster than 2475 at 4000 A. It was not used in this experiment, although it will probably be tried in the future. In an attempt to capture the near-infrared region, a short length of Kodak High Speed Infrared Film was placed in the 7000-7800 A portion of the spectrograph camera. This met with no success (negligible density change) and the cause appears to be reciprocity failure in the red-sensitive emulsion since good exposures were obtained from the standard lamp. However quantitative work needs to be done before definite statements can be made.

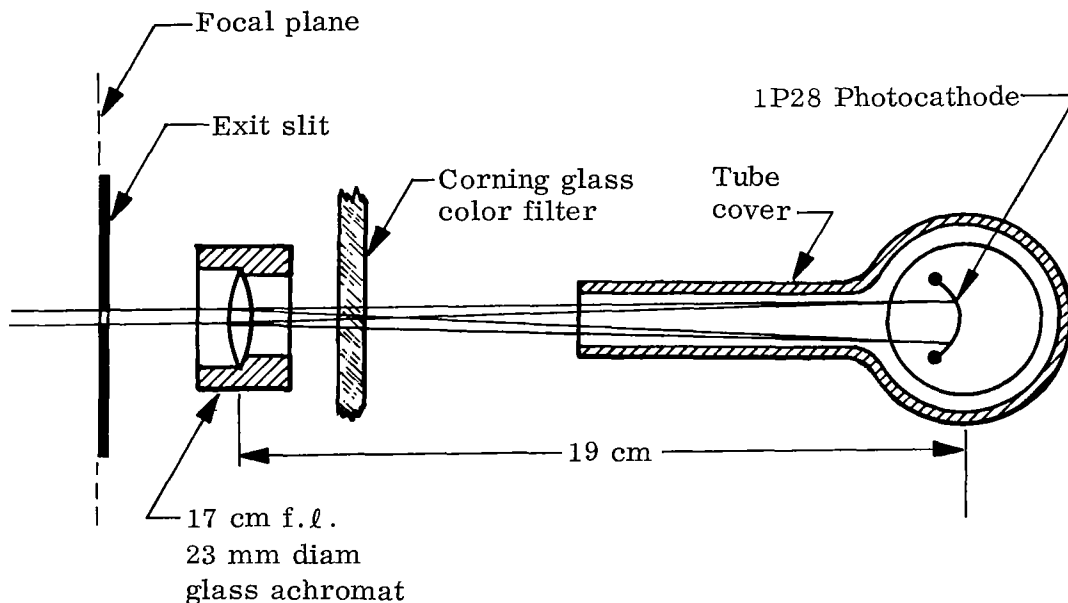
Polychromator

The polychromator was used to measure photoelectrically the absolute intensities averaged over 5-50 A spectral intervals at selected wavelengths in the visible spectrum. As mentioned earlier, the basic instrument was another JACO 1.5 m Wadsworth Spectrograph. A large (1 x 1.5 x 2 ft), light-tight box was added at the camera end so that phototubes could be conveniently located

* Kodak literature for the 2475 film (Pamphlet No. P-95) indicates that deviations between 10^{-4} sec and 0.16 sec are negligibly small ($\sim 10\%$).

behind the focal plane. The polychromator was coupled to the shock tube by the optical system shown on Fig. 5. Again the requirement was for a narrow beam along the tube diameter but in addition the system had to form a small image of the entrance slit in the center of the tube for calibration purposes. The overall length of the system was much longer than that of the spectrograph (Fig. 2) because of physical space limitations. Glass lenses were used because radiation below 3500 Å was of no interest here. The polychromator field of view was directly opposite to that of the spectrograph so that both instruments viewed the same gas sample, but from different ends.

Five, fixed-type exit slits were mounted along the focal plane. So that the photocathode of each photomultiplier tube would be uniformly irradiated regardless of the spectral energy distribution across each exit slit, the system sketched below was employed.



Top view of component arrangement behind focal plane of polychromator.

Here light emergent from each slit was collected by the 17 cm f.l. achromats which formed 1/8-size images of the grating on the photocathodes of 1P28 photomultiplier tubes. Corning glass color filters were used to block

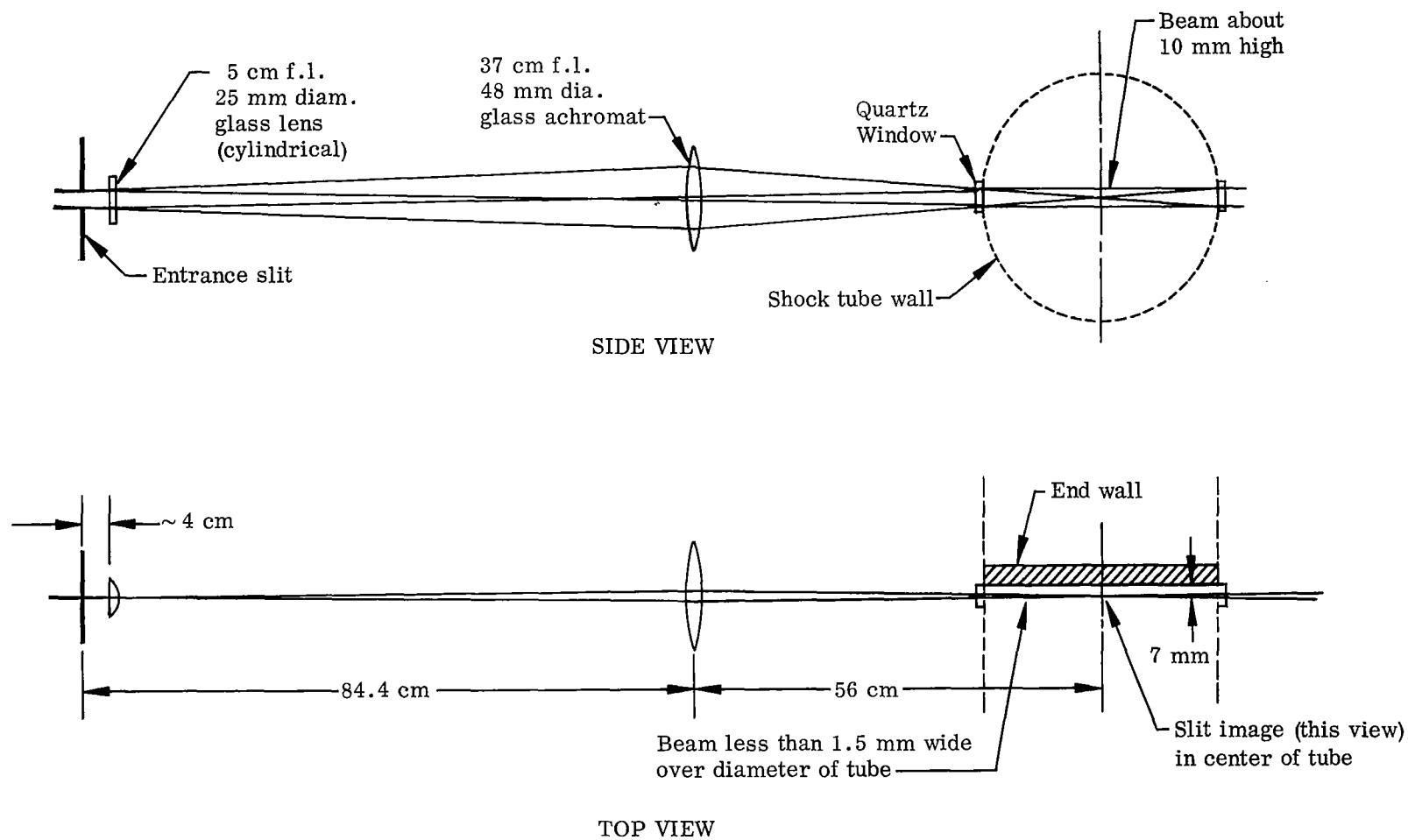
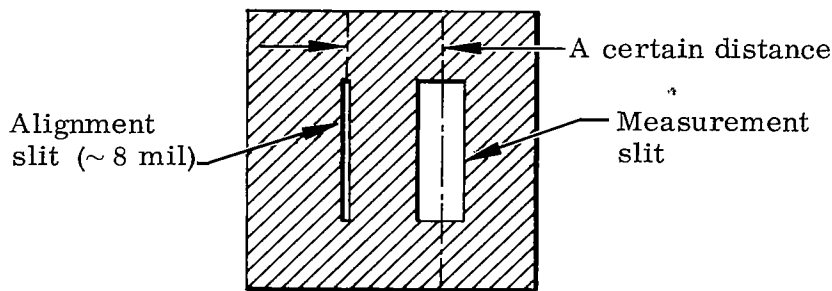


Fig. 5 Optical System for Polychromator

scattered light and (in one instance) second-order spectra. The open spaces between each exit slit were covered with black photographic tape so that the only light entering the light-tight box had to come through an exit slit. The phototubes were collimated as shown to eliminate possible cross talk. The phototubes were culled from a large supply by selecting those which exhibited the best signal/noise ratios at the wavelengths of interest.

The factors governing the selection of the center wavelength and spectral bandpass for each exit slit will be discussed later and here these values are assumed to be given. The technique used to locate these slits was to have a second alignment slit cut in the same piece of metal. A nearby, strong reference line from the spectra of Hg, A, He, or Ne was selected for this alignment. This line, together with the above values and the measured (photographically) reciprocal linear dispersion gave the necessary input to design an exit slit similar to that sketched below.



Sketch of fixed exit slit used in polychromator

The exit slits were milled from 0.010-inch hard aluminum sheets about 1.5 inches square. The exact widths and separation were determined by measurement on an optical comparator.

The slits were clamped along the focal plane by screws and washers to permit adjustment. Alignment was accomplished by locating the appropriate reference line in the field of a short-focus telescope and then manipulating the exit slit until this reference line was in the center of the alignment slit when the exit slit was locked tight. With a $50\text{ }\mu$ entrance slit, the width of this reference line was $50\text{ }\mu$ or 2 mil. An easily observable misalignment would be

2 mil which is equivalent to 0.5 Å in wavelength along the focal plane. Thus the exit slits could be located in the above manner to better than ± 0.5 Å.

Polychromator Calibration and Analysis

The polychromator system was calibrated by replacing the unknown reflected shock plasma with a source of known spectral intensity. This was an Eppley Standard of Spectral Radiance - a General Electric 30A/T24/7 tungsten ribbon filament lamp calibrated by Eppley from 0.25 to 0.75 μ at 35 amps. In practice a similar lamp was used as a working standard. The lamps were placed at the center of the shock tube where the slit image was comfortably smaller than the filament. Thus the system was calibrated through the same lenses, windows, etc., as used for each shot. This did mean that the calibration had to be performed hours before each shot - before the tube was closed and evacuated. However with one exception, the calibrations did not change significantly from day to day so this was not a serious disadvantage.

To provide a periodic calibration light signal, a 3600 rpm chopper was placed immediately in front of the entrance slit. The chopper blade was 5.2 inch diameter and contained a single slit 0.050 inch wide. This yielded a flat-topped 50 μ sec light pulse every 1/60 sec and hence provided a fair simulation of the time behavior of the transient light pulse from the reflected shock region.

The amplitudes of the plasma light pulses were from 50-5000 times greater than that of the standard lamp and thus the linearity of the photomultiplier tubes was an important consideration. Linearity was established over the full range by replacing the standard lamp with a Xenon flash tube and inserting various neutral density filters into the optical path. The amplitude disparity was slightly reduced by opening the polychromator entrance slit to 300 μ during calibration (the slit image remained sufficiently narrow) which gave a sixfold increase in the energy received by each phototube. The principal advantage of this was to improve the signal/noise ratio of the calibration signals. The exact factor was measured by using the zero-order light and it appeared to hold for all the phototubes.

The equation for the rate at which energy passes through an exit slit on the polychromator focal plane is readily derived by rewriting Eq. (3) in terms of a focal plane heat flux. However for this application the instrument function describes the appearance of a monochromatically-irradiated entrance slit in the focal plane. From the earlier results, this is merely the geometric image of the entrance slit and thus the focal plane heat flux becomes

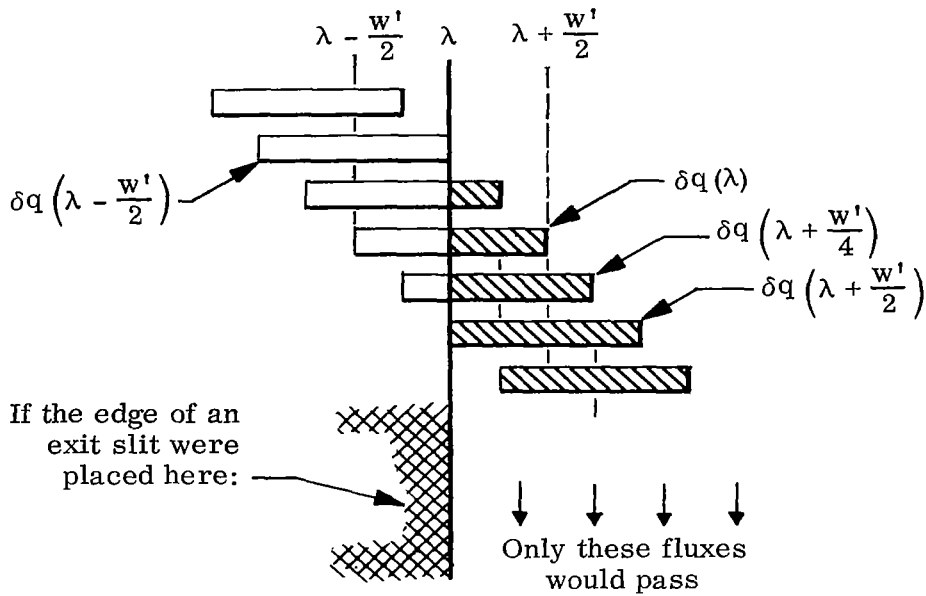
$$q(\lambda) = \frac{A}{f^2} \tau(\lambda) \int_{\lambda - \frac{W'}{2}}^{\lambda + \frac{W'}{2}} I_{\lambda}(\lambda') d\lambda \quad (6)$$

This is the heat flux at a particular point on the focal plane and it receives contributions from wavelengths $\lambda \pm W'/2$ where W' is the spectral width of the entrance slit.

The contribution from each wavelength is obtained by differentiating the above equation whereupon

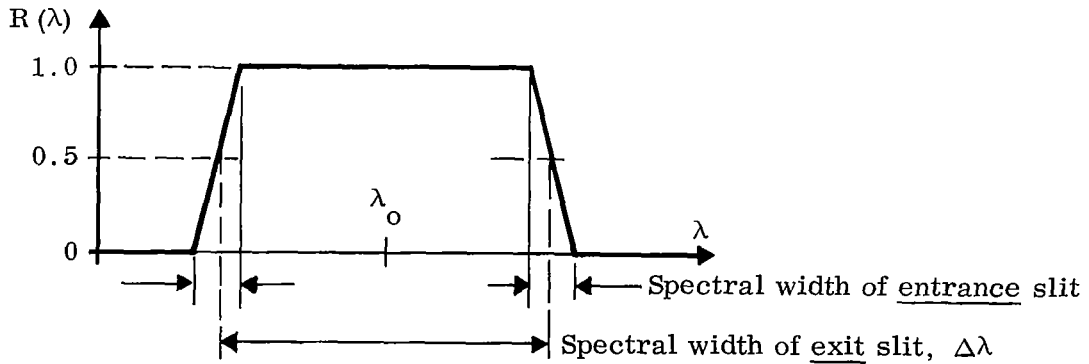
$$dq(\lambda) = \frac{A}{f^2} \tau(\lambda) I_{\lambda}(\lambda) d\lambda \quad (7)$$

Here $dq(\lambda)$ represents the incremental heat flux resulting from the monochromatic intensity $I_{\lambda}(\lambda)d\lambda$. This flux is uniform over the entrance slit image which occupies a distance W or spectral interval $W' = W(RLD)$ along the focal plane. The distribution of these differential heat fluxes is best shown graphically. The sketch on the next page indicates how an edge of the exit slit masks a portion of the images resulting from wavelengths near that of the exit slit edge. The situation for the other edge would, of course, be similar. This sketch considers intervals $d\lambda = W'/4$ for clarity.



Schematic representation showing passage of differential fluxes by an exit slit edge.

To obtain the rate at which energy passes through an exit slit, the areas have to be modified to account for this masking effect. This is accomplished by the weighting function $R(\lambda)$ sketched below.



Exit slit weighting function.

Now the differential rate for the energy passed by an exit slit is given by $de(\lambda) = dq(\lambda) A_s R(\lambda)$ and, by integrating over the nonzero limits of $R(\lambda)$, the total rate E is

$$E(\Delta\lambda) = \frac{AA_s}{f^2} \int_{\Delta\lambda+W'} I_\lambda(\lambda) R(\lambda) \tau(\lambda) d\lambda \quad (8)$$

The weighting function only involves the intensities near the exit slit edges and these edges were placed in spectral regions where the variations of the spectral intensity with wavelength were small. By neglecting these small variations, the weighting function $R(\lambda)$ can be "squared up" and further by assuming the transmission to be constant over the entire exit slit width, the above equation can be simplified to yield

$$E(\Delta\lambda) \cong \frac{AA_s}{f^2} \tau(\lambda) \int_{\lambda_o - \frac{\Delta\lambda}{2}}^{\lambda_o + \frac{\Delta\lambda}{2}} I_\lambda(\lambda) d\lambda \quad (9)$$

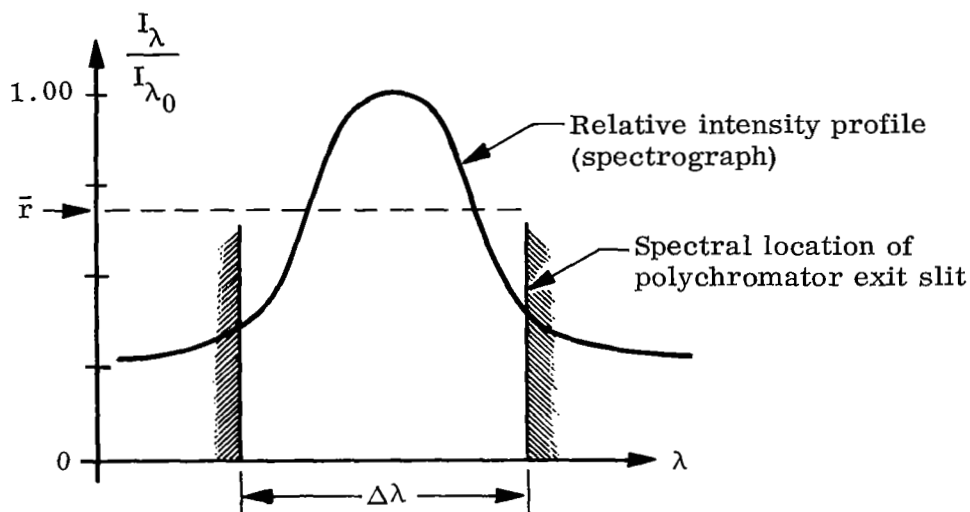
During the polychromator calibration the source was a standard lamp whose spectral intensity varied slowly and smoothly with wavelength. By choosing a mean value the following operational equations for the polychromator can be derived from Eq. (9):

$$I_{\Delta\lambda} = I_\lambda (\text{std. lamp}) \frac{V_{\text{plasma}}}{V_{\text{std. lamp}}} = \frac{1}{\Delta\lambda} \int_{\Delta\lambda} I_\lambda d\lambda = \frac{I_{\lambda_o}}{\Delta\lambda} \int_{\Delta\lambda} \left(\frac{I_\lambda}{I_{\lambda_o}} \right) d\lambda \quad (10)$$

Here $I_\lambda(\text{std. lamp})$ is the mean spectral intensity of the standard lamp and $V_{\text{plasma}}/V_{\text{std. lamp}}$ is the ratio of the shot signal to the calibration signal obtained from a given photomultiplier tube. Thus $I_{\Delta\lambda}$ is the mean spectral intensity of the plasma averaged over the spectral width of the exit slit as given by the third equality. The fourth equality was obtained by inserting a normalizing constant I_{λ_o} to make the integrand resemble the relative spectral intensity profile as obtained by the spectrographic techniques discussed earlier. The above equations represent the limit of the simplification of the polychromator results without further knowledge concerning the spectral nature of the plasma radiation.

Combination of Results from Spectrograph and Polychromator

The spectrographic results provide this detailed spectral information and can be used to perform the integration required by the last equality in Eq. (10). For the moment, changes in the spectral intensity over the width of the instrument function will be neglected so that the relative exposure profile can be considered equivalent to the relative spectral intensity profile. Thus the position of the exit slits can be drawn on the profile and, by planimetry, an average relative spectral intensity (\bar{r}) over $\Delta\lambda$ can be obtained as sketched below.



Sketch indicating the physical meaning of the average relative spectral intensity.

This operation yields, from the spectrographic result:

$$\bar{r} = \frac{1}{\Delta\lambda} \int_{\Delta\lambda} \left(\frac{I_{\lambda}}{I_{\lambda_0}} \right) d\lambda \quad (11)$$

and combining this with the appropriate polychromatic result from Eq. (10) yields

$$I_{\lambda_0} = \frac{I_{\Delta\lambda}}{\bar{r}} \quad (12)$$

This is an important equation because it provides absolute calibrations for the relative spectral intensity profiles from the spectrograph without having to perform quantitative photometry.

PLASMA THERMOMETRY

In this chapter the equations needed to calculate a plasma temperature from the polychromatic and spectrographic results are derived together with the appropriate error analyses.

General Error Analysis

Basically the plasma temperature was calculated from the measured value of a temperature-dependent radiative quantity M . Such a quantity, emitted by a steady isothermal plasma, will generally depend on the two thermodynamic variables which define the state of the plasma together with certain physical constants. By selecting temperature and pressure as the thermodynamic variables and denoting the lumped physical constants as C , this functional relationship can be expressed by $M = f(T, P, C)$. The total differential of this relation can be written in the following nondimensional form:

$$\frac{dT}{T} = \frac{\frac{dM}{M} - \frac{P}{M} \frac{\partial M}{\partial P} \Big|_{T,C} \frac{dP}{P} - \frac{C}{M} \frac{\partial M}{\partial C} \Big|_{T,P} \frac{dC}{C}}{\frac{T}{M} \frac{\partial M}{\partial T} \Big|_{P,C}} \quad (13)$$

Here the left side represents the uncertainty in the calculated temperature while the numerator on the right contains terms which describe the uncertainty in the measurement of M itself together with the effect of the uncertainty in the pressure and the lumped physical constants. The denominator will be called the temperature sensitivity and clearly it will mitigate the other uncertainties if it is large.

Thus the selection of the quantities M used to determine the plasma temperature depended in part on the temperature sensitivity. This in turn is a function of temperature and can limit the region of usefulness as will be demonstrated. For the lower plasma temperatures the shape and/or the total intensity radiated by certain atomic lines and multiplets were selected as suitable quantities.

Derivatives of Plasma Properties

To evaluate the temperature uncertainty resulting from the measurement of these quantities, certain partial derivatives of the plasma properties will be required.

The Saha equation and the equation of state for the singly-ionized region of a neutral, monatomic (or fully dissociated polyatomic) plasma of a single specie are:

$$\frac{\alpha^2}{1-\alpha} = \frac{U_+}{U} \left(\frac{1}{n_A + n_e} \right) A T^{3/2} \exp\left(-\frac{I}{kT}\right) \quad (14)$$

$$P = (2n_e + n_A) kT \quad (15)$$
$$\alpha \equiv \frac{n_e}{n_e + n_A}$$

where α is the degree of ionization, U_+/U is the ratio of the ion to neutral electronic partition functions, I is the ionization energy, $A = 4.83 \times 10^{15} \text{ cm}^{-3} \text{ K}^{-3/2}$, and n_e and n_A are the electron and neutral particle densities. These equations are given in Chap. 3 of Zel'dovich and Raizer.⁶

The requisite partial derivatives are obtained from these equations and can be expressed as follows:

$$\left. \frac{T}{n_e} \frac{\partial n_e}{\partial T} \right|_P = \left. \frac{T}{n_{A+}} \frac{\partial n_{A+}}{\partial T} \right|_P = \frac{1-\alpha}{2} \left(\frac{I}{kT} + \frac{5}{2} \right) - 1 \quad (16)$$

$$\left. \frac{T}{n_A} \frac{\partial n_A}{\partial T} \right|_P = -\alpha \left(\frac{I}{kT} + \frac{5}{2} \right) - 1 \quad (17)$$

$$2 \left. \frac{P}{n_e} \frac{\partial n_e}{\partial P} \right|_T = \left. \frac{P}{n_A} \frac{\partial n_A}{\partial P} \right|_T = 1 + \alpha \quad (18)$$

Since $\alpha = f(T, P)$, these derivatives are functions of temperature and pressure.

While the Saha equation is not strictly valid for air, it is noted that if $U_+/U = 0.77$ and $I = 13.8$ eV are used in Eqs. (14) and (15), the resultant values for the degree of ionization are within 1% of the values calculated from the data in Table A2 where $\alpha = 0.01$ to 0.5. This is excellent agreement for the intended purpose. Thus the above partial derivatives were evaluated along the path of the reflected shock Hugoniot states (ref. Table A2) by using $I = 13.8$ eV and the tabular values of the degree of ionization. The resulting curves are shown in Fig. 6 and will be used in the discussions which follow. The curves apply to either nitrogen or oxygen atoms because of the assumptions involved.

Radiant Energy Transport Equations

The basic equation for radiation transport in an isothermal plasma is

$$I_\lambda = B_\lambda \left[1 - e^{-\mu_\lambda \delta} \right] \quad (19)$$

where I_λ is the specific intensity, δ the pathlength, and μ_λ the spectral absorption coefficient which contains additive contributions from all line ($\Sigma \mu_\lambda^L$) and continuum (μ_λ^C) radiation. B_λ is the Planck function which, for wavelengths in microns, is given by

$$B_\lambda = \frac{1.191 \times 10^4}{(\lambda)^5} \frac{1}{\exp\left(\frac{C_2}{\lambda T}\right) - 1}, \frac{W}{\text{cm}^2 \text{sr-}\mu} \quad (20)$$

where $C_2 = 1.439 \times 10^4$ μK .

Inverting the basic transport equation (Eq. 19) yields

$$\mu_\lambda = \Sigma \mu_\lambda^L + \mu_\lambda^C = -\frac{1}{\delta} \ln \left[1 - \frac{I_\lambda}{B_\lambda} \right] \quad (21)$$

For line radiation, the integrated absorption is defined as

$$\Phi = \int_0^\infty \mu_\lambda^L d\lambda \quad (22)$$

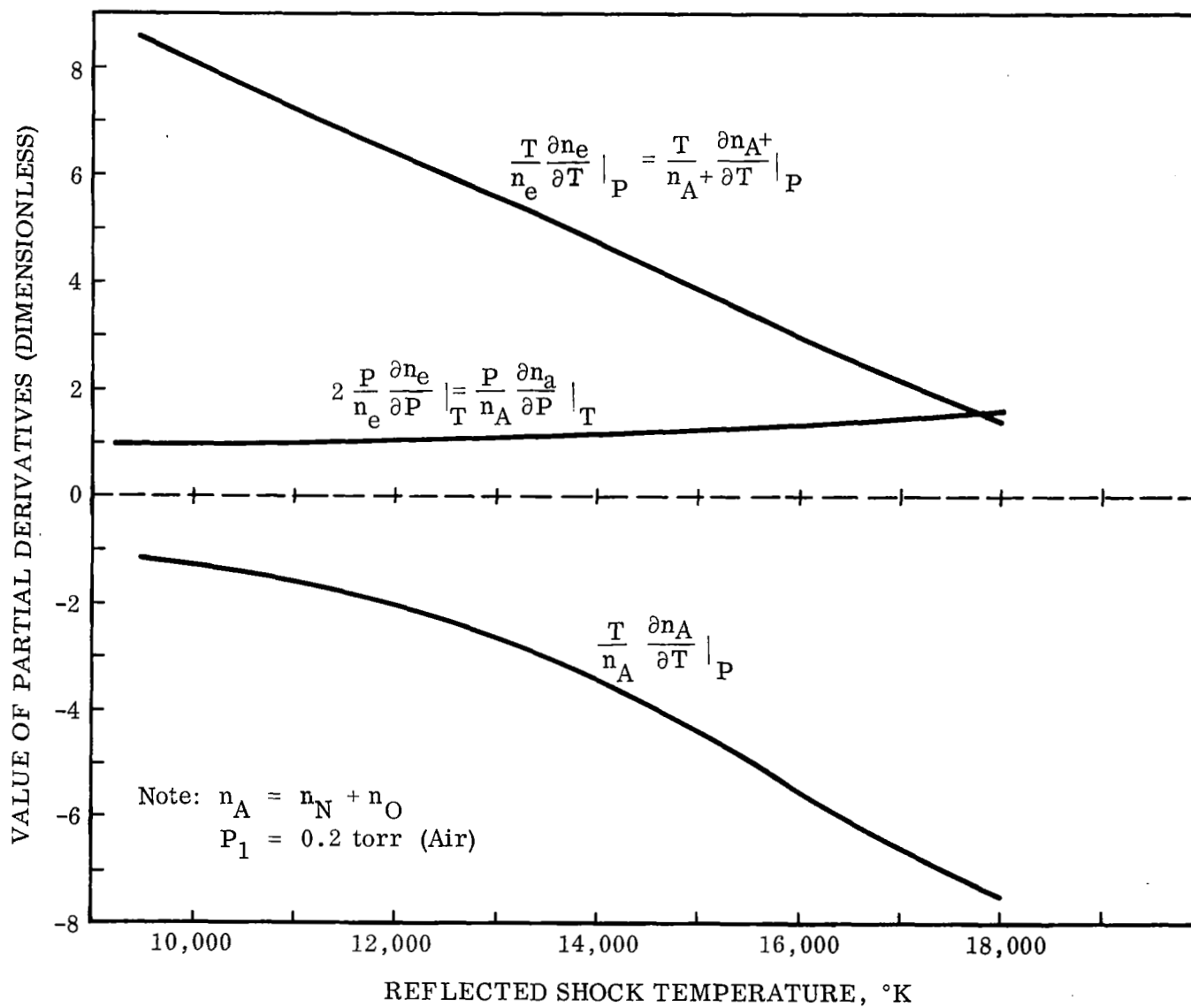


Fig. 6 Partial Derivatives of Plasma Properties Evaluated Along the Reflected Shock Hugoniot

where μ_{λ}^I now refers to contributions from a particular line or multiplet only. For wavelengths in microns, the integrated absorption is:

$$\oint = \left[1 - \exp\left(-\frac{C_2}{\lambda T}\right) \right] \left[\frac{1.10 \times 10^{-16}}{1.2406} (\lambda)^2 (gf) \frac{n_i}{\Sigma_i} \exp\left(-\frac{\epsilon_l}{kT}\right) \right], \text{ cm}^{-1}\mu \quad (23)$$

where n_i is the number density of the emitting specie in part./cm^3 , Σ_i the partition function, g the lower state degeneracy, f the f -number, and ϵ_l the lower state energy. The last three parameters were taken from the NBS tables⁷ whenever possible. These equations, together with the combined results from the polychromator and spectrograph, were used to determine a temperature from the measured intensity of a particular line or multiplet as outlined below.

Thermometry of Line Intensity Measurements

The required numerical work was done by a digital computer code originally written to analyze line radiation that was not optically thin. However since it is valid for any opacity, its use became routine despite the fact that simpler expressions can be written when opacity effects are negligible. Basically the integrated absorption (Eq. 22) was computed from experimental measurements of a given line or multiplet. Then this value was used to determine a temperature by numerical inversion of Eq. (23).

The pertinent experimental results were the relative intensity profile from the spectrograph (see sketch on p. 27) together with the value of the normalizing intensity as obtained from the combined result from the spectrograph and polychromator (Eq. 12). This experimental profile contains contributions not only from the line or multiplet under consideration but also from the continuum and possibly other multiplets.* These contributions must be separated and this becomes increasingly difficult at the higher temperatures. Examples of this separation will be given in the next chapter.

*The continuum, as used here, means an unchanging spectral intensity and could very well include the underlying wings of other multiplets.

For the moment, consider this separation accomplished and select two wavelengths λ_1 and λ_2 on opposite sides of a given multiplet where the spectral absorption coefficient of the multiplet is effectively zero and where the continuum intensity (I_λ^C) can be determined. Equations (21) and (22) can now be combined to yield

$$\oint = -\frac{1}{\delta} \int_{\lambda_1}^{\lambda_2} \ln \left[1 - \left(\frac{I_{\lambda_0}}{B_\lambda} \right) \left(\frac{I_\lambda}{I_{\lambda_0}} \right) \right] d\lambda - \mu_\lambda^C (\lambda_2 - \lambda_1) \quad (24)$$

where

$$\mu_\lambda^C = -\frac{1}{\delta} \ln \left[1 - \left(\frac{I_{\lambda_0}}{B_\lambda} \right) \left(\frac{I_\lambda^C}{I_{\lambda_0}} \right) \right]$$

Here spectral changes in the Planck function, continuum intensity, and normalizing factor have been neglected.

The computational scheme was to input the normalizing factor (Eq. 12), the relative intensity profile, and a first estimate of the plasma temperature which was used to evaluate the Planck function. The computer calculated a value for the integrated absorption (Eq. 24) utilizing Simpson's rule and then, by iteration, found the temperature that satisfied Eq. (23). This temperature was generally not equal to the first estimate, so a second estimate was made and this procedure continued until the two temperatures agreed. The printout included the continuum spectral absorption coefficient (μ_λ^C) and the peak emissivity (I_{λ_0}/B_λ) and these are noteworthy because of the consistency checks they provide as discussed later. These computations were performed on a time-sharing digital computer (TYMSHARE).

Up to this point the effects of the instrument function and the exit slit weighting function have been tacitly neglected. The exit slit weighting function can be "squared up" (Eq. 9) without introducing a significant error provided the spectral intensity did not change rapidly at the exit slit edges. The slits were located so that this was generally true. The effect of the instrument function can be assessed by first recalling that broadening does not destroy energy. Thus in general the main effect of treating a relative exposure profile as a relative intensity profile is that the normalizing

intensity I_{λ_0} (Eq. 12) is too low. This error is partially cancelled in the subsequent spectral integration process and it can be shown that there is no resultant error when the radiation is optically-thin. When opacity effects become important, the errors do not completely cancel but at the same time, opacity effects are concurrent with higher temperatures, electron densities, and hence broader lines whereupon the instrument function itself becomes less important. Thus in summary the effects of the instrument function and exit slit weighting function were negligible when spectrally-integrated quantities were used as was the case in this thermometric technique.

Error Analysis for Line Intensity Thermometry

To obtain analytic expressions for the temperature uncertainties, the radiation must be assumed to be either optically-thin or optically-thick. Since the experimental conditions were more nearly optically-thin and since it can be shown that the optically-thick case yields only slightly greater temperature errors, only the optically-thin case will be treated here.

The optically-thin assumption ($I_{\lambda} \ll B_{\lambda}$ or $\mu_{\lambda} \delta \ll 1$) permits the integration of Eq. (24) by the expansion $\ln(1-x) \cong -x$ with the result:

$$\int_{\lambda_1}^{\lambda_2} I_{\lambda} d\lambda = \delta B_{\lambda} \delta + I_{\lambda}^C (\lambda_2 - \lambda_1) \quad (25)$$

The measured quantity M is considered to be the integrated line intensity $\delta B_{\lambda} \delta$. The continuum contribution will be treated as a constant because its magnitude was not used to determine a temperature in this thermometric technique.

Combining Eq. (23) with the Planck function (Eq. 20) yields the integrated line intensity

$$\delta B_{\lambda} \delta = 1.056 \times 10^{-12} \frac{\delta}{(\lambda)^3} (gf) \frac{n_i}{\sum_i} \exp\left(-\frac{\epsilon_u}{kT}\right), \text{ W/cm}^2\text{sr} \quad (26)$$

where ϵ_u is the upper state energy. Substituting this expression into Eq. (13) and performing the required differentiation yields the following expression for the uncertainty in the measured temperature:

$$\frac{dT}{T} = \frac{\frac{d(\delta B_{\lambda})}{\delta B_{\lambda}} - \frac{P}{n_i} \left. \frac{\partial n_i}{\partial P} \right|_T \frac{dP}{P} - \frac{df}{f}}{\frac{T}{n_i} \left. \frac{\partial n_i}{\partial T} \right|_P - \frac{T}{\Sigma_i} \frac{d\Sigma_i}{dT} + \frac{\epsilon_u}{kT}} \quad (27)$$

The temperature sensitivity of this technique is given by the denominator which represents the change of the excited state population with temperature. For most visible transitions of NI or OI, the upper state energy ϵ_u is about 13 eV. The derivative of the partition function is small (≈ 0.5) and changes slowly. However the first term, representing the change in the neutral number density, is negative and becomes large at the higher temperatures (ref. Fig. 6). Thus the temperature sensitivity decreases rapidly at the higher temperatures and the result of this will be demonstrated shortly.

The first term in the numerator describes the uncertainty in the experimental measurement of the integrated line intensity which, for optically-thin conditions, is given by Eq. (25). However the actual determination is better described by referring again to the sketch on p. 27. The polychromatic result provides the absolute value of the integral of the spectral intensity over the width of the exit slit. From Eq. (10), the uncertainties in this value stem from those of the standard lamp intensity ($\pm 2\%$), the measurement of the standard lamp signal voltage ($\pm 3\%$), and the measurement of the plasma signal voltage ($\pm 5\%$) and when added together, give a total uncertainty of $\pm 10\%$ to the polychromatic result.

Then two corrections were applied to this result and both were derived from the relative spectral intensity profile. First an additive correction was applied to account for the line wings cut off by the exit slit and, for the wide slits used herein, this was a relatively minor correction. The second and more important correction was a subtraction of the continuum contribution

and this involved first an estimate of the apparent continuum level from the relative intensity profile. Through experience gained during the shape-fitting procedures discussed next, this level could be picked to ± 0.02 units of relative intensity. Finally deviations between this relative intensity level and the actual plasma emission must be considered. By definition this deviation is zero at $I_\lambda/I_{\lambda_0} = 1.0$ but lower values involve the H-D curve and the attendant effects of film noise, weak exposures, and the assumptions of homochromatic photometry. Quantitatively, these effects are described by the following equation derived from practical experience:

$$\Delta \left(\frac{I_\lambda}{I_{\lambda_0}} \right) \approx \pm 0.04 \left(1 - \frac{I_\lambda}{I_{\lambda_0}} \right) \quad (28)$$

where the left hand side represents the deviations between the actual plasma emission and the relative intensity profile.

The effect of these two corrections was quantified by assuming a reasonable line shape and exit slit width and various continuum levels. The results indicated that these spectrographically-derived corrections to the polychromatic result added another $\pm 10\%$ uncertainty if the continuum level was below $0.5 I_{\lambda_0}$ and that the uncertainty rose rapidly if the continuum level was higher. This latter behavior occurs because the process of subtracting the continuum yields a result for the integrated line intensity which is the difference between two large numbers, each of which has an associated uncertainty.

Thus the first term in the numerator of Eq. (27) is estimated to be $\pm 20\%$ at low continuum levels. The second term contains a derivative which is near unity (ref. Fig. 6) and the pressure itself which is considered uncertain to $\pm 10\%$ since it was not measured during this experiment. The third term represents the uncertainty in the f-number which for NBS grade B lines⁷ is $\pm 10\%$. Hence the numerator of Eq. (27) becomes $\pm 40\%$ and, when divided by a typical temperature sensitivity of 10 at 12,000 K, indicates a temperature uncertainty of $\pm 4\%$.

At 15,000 K, the temperature sensitivity drops to about 4.5 which would yield a temperature uncertainty of $\pm 9\%$ even if the continuum level stayed below 50% which, as will be shown later, it does not. Hence the thermometric technique of measuring the integrated intensity of an NI or OI line is fairly precise for temperatures up to about 13,000 K, but this precision is rapidly lost at higher temperatures both because of a loss in temperature sensitivity and because of the high continuum levels.

Thermometry of Line-Shape Fitting

The shapes of well-known atomic lines provided the other plasma thermometer used during this experiment. The fitting process was done essentially by choosing a set of plasma properties, computing the resultant relative intensity profile, broadening this by the instrument function, and comparing this against the measured relative exposure profile. Then the plasma properties were varied until a best fit to the experimental shape was obtained. This procedure included the effects of finite opacity and involved the whole experimental shape rather than just the half-width. The derivation below applies to a single line from neutral atomic nitrogen which has a Lorentzian shape.* Other atoms and shapes were dealt with in a similar manner.

The line shape is normally characterized by a half half-width γ . For neutral nitrogen, the temperature and electron density dependence are given by Page et al.⁸ as:

$$\gamma = K T^{1/4} n_e \quad (29)$$

The proportionality constant K was obtained from the tabulations of Wilson and Nicolet.⁹ The computation began by picking first-estimate values of T , n_e , and n_N . These three parameters were evaluated at the same reflected shock Hugoniot state (ref. Table A2) and so, for iterative purposes, they can be considered as a single variable. For Lorentzian lines and neglecting shifts, the spectral absorption coefficient is given by

*The effects of Doppler broadening were negligible for the conditions of this experiment.

$$\mu_{\lambda}^L = \frac{\mu_{\lambda_0}^L}{\left(\frac{\lambda - \lambda_0}{\gamma}\right)^2 + 1}, \quad \mu_{\lambda_0}^L = \frac{\$}{\pi\gamma} \quad (30)$$

where $\$$ is the integrated line absorption (ref. Eq. 23).

Now to generate a spectral intensity, the continuum must be included. This was done by estimating the relative intensity of the continuum, C , defined as $C = I_{\lambda}^C / I_{\lambda_0}$. Rewriting this expression in terms of absorption coefficients (ref. Eq. 19) yields

$$1 - \exp(-\mu_{\lambda}^C \delta) = C \left[1 - \exp[-(\mu_{\lambda_0}^L + \mu_{\lambda}^C) \delta] \right] \quad (31)$$

which can be solved explicitly for μ_{λ}^C . This value, together with the line absorption coefficient (Eq. 30) permits computation of the relative spectral intensity profile by the relation

$$\frac{I_{\lambda}}{I_{\lambda_0}} = \frac{1 - \exp[-(\mu_{\lambda}^L + \mu_{\lambda}^C) \delta]}{1 - \exp[-(\mu_{\lambda_0}^L + \mu_{\lambda}^C) \delta]} \quad (32)$$

To compare this theoretical profile to the experimental relative exposure profile, the instrument function cannot be neglected since spectral shape is now an important parameter. The above theoretical intensity profile was numerically broadened using Eq. (4) and the instrument function shown on Fig. 1. Thus a theoretical relative exposure profile was generated based on assumed values of the parameters T , n_e , n_N , and C .

The criterion used to determine the quality of the fit was based on the RMS value between about 10-20 points taken from the experimental profile and the theoretical values generated at corresponding wavelengths (ref. Eq. 37 on p. 53). The iterative procedure consisted of varying the two input parameters (i.e. (T, n_e, n_N) and C) until a minimum RMS value was found. As shown later, these minimum values corresponded to an average difference of .01-.04 units of relative exposure which is in good agreement with the uncertainty given by Eq. (28).

The dependence of this fitting procedure on such intensity-governing parameters as the nitrogen number density and f-number is rather weak. This can be demonstrated readily by again making the assumption that the radiation was optically thin. By working backwards through Eqs. (32), (31), and (30), the following relation is readily obtained:

$$\frac{I_{\lambda}}{I_{\lambda_0}} = \frac{1 + C\left(\frac{\lambda - \lambda_0}{\gamma}\right)^2}{1 + \left(\frac{\lambda - \lambda_0}{\gamma}\right)^2} \quad (33)$$

Here it is clear that the optically-thin shape is dependent only on the continuum level (which is perturbed), the wavelengths (which are considered precisely known), and the half half-width which, from Eq. (29), depends weakly on temperature and linearly on electron density. Thus the other thermodynamic parameters enter only through consideration of a finite opacity and this was usually a relatively unimportant (but nonnegligible) effect.

This shape fitting procedure was applied not only to neutral nitrogen but also to the $H\alpha$ line (6563 Å) which was present as an impurity. This presented three complications. First the shape is not Lorentzian and is given in tabular form by Griem.¹⁰ This was handled by a program option in the computer and presented no great difficulty. Secondly, because hydrogen was an impurity, the number density could not be obtained as before. Instead it was determined from a peak spectral intensity obtained using the spectrographic results to scale a 6488 Å polychromatic measurement of a nitrogen multiplet. This was an uncertain number but recall that the number density is relatively unimportant provided opacity effects are small. Finally a controversy exists as to whether the Griem¹⁰ shapes correctly represent $H\alpha$. Morris et al.¹¹ have calibrated $H\alpha$ against the better-known values of $H\beta$ and report that the Griem values for the $H\alpha$ half-width are too narrow by 28% at $n_e = 10^{16}$ and by 14% at $n_e = 10^{17} \text{ cm}^{-3}$ and cite corroborating results by Wiese at NBS. The $H\alpha$ shape fitting was done using both shape values but as will be seen, this experiment cannot shed light on this controversy.

Error Analysis of Line-Shape Thermometry

For the purpose of this analysis, the measured quantity will be taken to be the line half half-width as given by Eq. (29). Substituting this expression into Eq. (13) and performing the required differentiation yields:

$$\frac{dT}{T} = \frac{\frac{d\gamma}{\gamma} - \frac{P}{n_e} \left. \frac{\partial n_e}{\partial P} \right|_T \frac{dP}{P} - \frac{dK}{K}}{\frac{1}{4} + \frac{T}{n_e} \left. \frac{\partial n_e}{\partial T} \right|_P} \quad (34)$$

Here, as before, the temperature sensitivity drops sharply with temperature (ref. Fig. 6) which in this case reflects the fact that the electron density is a slowly changing function of temperature at the higher temperatures. The proportionality constant K is known to about $\pm 20\%$ for visible nitrogen lines and a $\pm 10\%$ pressure uncertainty only contributes about $\pm 5\%$ to the temperature uncertainty because the derivative is about 0.5 (ref. Fig. 6).

To obtain the uncertainty in the half half-width measurement, it is necessary to again assume optically-thin conditions. Then Eq. (33) is applicable and, by considering I_λ/I_{λ_0} , λ , and C as the independent variables, the total differential of γ can be obtained by straightforward differentiation. The uncertainty in the relative intensity is given by Eq. (28) which was shown to yield reasonable values and, because the continuum was perturbed during the fitting process, it can be considered known to ± 0.005 units of relative intensity. Inserting these uncertainties into the total differential of yields:

$$\frac{d\gamma}{\gamma} = \frac{1}{2} \frac{1 \pm 0.04 \frac{(1-C)}{\left(\frac{I_\lambda}{I_{\lambda_0}} - C\right)} \pm 0.005}{\left(\frac{I_\lambda}{I_{\lambda_0}} - C\right)} + \frac{d\lambda}{\lambda - \lambda_0} \quad (35)$$

This yields the uncertainty in γ resulting from a single measurement point. However the measurement was not done at a single point but rather at many throughout the profile. It is assumed that the overall uncertainty is typical

of the value at the half-intensity point of the line contribution, i.e.

$I_\lambda/I_{\lambda_0} = C + 0.5 (1-C)$ where $\gamma = \pm (\lambda - \lambda_0)$. With these assumptions, the above equation becomes

$$\frac{d\gamma}{\gamma} = \frac{\pm 0.04 (1-C) \pm 0.005}{1-C} \pm \frac{d\lambda}{\gamma} \quad (36)$$

The wavelength uncertainty will now be neglected; it was carried this far to indicate that very narrow lines can cause difficulty. The remaining expression yields errors of $\pm 4.5\%$ at $C = 0$, $\pm 5\%$ at $C = 0.5$, and $\pm 6\%$ at $C = 0.75$. This latter value can be unrealistic because high continuum levels imply large overlap and often increase the difficulty of separating one line from another. This source of uncertainty was not included in the error analysis. With this reservation in mind, the uncertainty in the half half-width measurement will be taken to be $\pm 5\%$.

Thus the temperature uncertainty resulting from the shape-fitting process on nitrogen lines was $\pm 4.5\%$ at 12,000 K and this rises to $\pm 7\%$ at 15,000 K. As will be shown in the next chapter, the broadening and attendant overlap at the higher temperatures made it difficult to maintain the $\pm 5\%$ measurement uncertainty. Thus both quantitatively and in the difficulties experienced at the higher temperatures, this thermometric technique was similar to that of the line intensity measurements discussed previously.

For $H\alpha$, the shapes are somewhat better known but since $\gamma \propto (n_e)^{2/3}$, the temperature sensitivity is reduced by $2/3$ with the result that the temperature uncertainties from the $H\alpha$ measurement are quite comparable to those of the nitrogen lines discussed above.

This discussion completes the derivation of the requisite analytical equations to measure the plasma temperature and analyze the resultant errors.

SPECTRAL SURVEYS

The next chapter will discuss the results of the plasma temperature measurements. However before the equations of the preceding chapter could be applied, the features of the emergent radiation were identified and it was shown that this radiation was indeed constant with time.

Spectral Identification

The first stage of the spectral work involved the identification of the various spectral features using time-resolved spectrograms. The microdensitometer traces from three such spectrograms are shown on Fig. 7 and are representative of a very low, an intermediate, and a high incident shock velocity. The ordinate on these traces is optical density and recall that this is related to the relative spectral exposure (or intensity) in a nonlinear way through the H-D curves. These spectrograms were taken early in the contractual year and used glass optics and an unblocked second order. Spectrograms obtained later with quartz optics and blocked second order were essentially identical in the region shown. The 2500-3400 Å region available with quartz optics showed very little of interest - no prominent lines and a smooth continuum. The light leak apparent at the red end of the middle trace on Fig. 7 was traced to the spectrograph housing and was repaired.

The three traces on Fig. 7 contain a great deal of qualitative information about the plasma radiation. First note that while the temperature increases relatively slowly, the electron density increases by factors of 5 or 6 between each trace. The bottom trace shows a considerable amount of molecular band radiation which was primarily from the N_2^+ (1st neg.) system. The band heads of the N_2 (2nd pos.) system are also discernable but considerably less pronounced. The top two traces clearly show the presence of continuum radiation but even qualitative statements about the spectral behavior are difficult to make - note the similarity between these traces and the spectral sensitivity of the 2475 film (Fig. 4).

The character of the line radiation is most interesting. On the bottom trace, the lines are generally prominent and narrow. On the middle trace they are still prominent but considerably broader and many more lines and multiplets are apparent, especially in the 5-6,000 Å region. Finally on the top trace the lines have become broad, the continuum has come up rapidly, and many lines are difficult to see above the continuum. Much of the structure in the 5-6,000 Å region has disappeared. The OI^{10} (6157) multiplet is interesting because it undergoes a 20 Å shift toward the red and becomes noticeably asymmetric.

This rapid rise of the continuum as the temperature increases can be qualitatively explained from theory. In the last chapter assuming (1) optically-thin, (2) visible region, and (3) temperatures about 12,000 K, it was shown that the temperature sensitivity for the integrated line intensity was 10 (ref. Eq. 27). But because the lines are becoming broader at the same time, the spectral intensity at the line centers does not increase nearly as rapidly. In fact for optically-thin Lorentzian lines, the temperature sensitivity of the spectral intensity at the line center is only 3.5 which is the difference between that of the integrated intensity (10 typ.) and the half half-width (6.5 typ.). (This can be readily shown from Eq. 30 et al.) Retaining the above assumptions it can be shown that the temperature sensitivity for the continuum (both recombination and negative ion attachment processes were included) is 10 at 12,000 K. Therefore on a spectral basis as represented by Fig. 7, the intensity at the line centers increases by $T^{3.5}$ while the continuum increases by T^{10} and thus the apparent submergence of the lines is not unexpected.

A listing of all the prominent multiplets and many of the lesser ones that have been identified at one time or another is given in Table 1. The identification process was greatly facilitated by a computer listing of the prominent lines and multiplets which gave quantitative criteria not found in finding lists or even multiplet tables. This listing was based on the NBS⁷ log gf data (if available) together with the half-widths and remaining gf data of Armstrong

TABLE 1. LISTING AND IDENTIFICATION OF PROMINENT AIR MULTIPLETS

Radiating Specie	Multiplet Number	Multiplet Wavelength	Theoretical Relative Strength	Identified?	Comments
NI	10	4107	1000	Yes	Much broader than predicted
NI	5	4222	600	Yes	
OI	*	6242	300	No	Never saw this one. NBS misprint?
NI	4	4256	300	Yes	
NI	6	4146	70	Yes	
OI	10	6157	40	Yes	Shifts to red, stands out
NI	9	4928	20	Yes	Two lines, 20 Å separation
NI	21	6490	20(x)	Yes	Looks broad, many lines
OI	6	3692	20(x)	Yes	Narrow and weak, often buried
OI	3	3947	20	Yes	
NI	13	5349	20	Yes	Many lines, widely spaced
NI	14	5295	20	Yes	
NI	20	6644	10	Yes	
OI	5	4368	10	Yes	Single line
NI	*	5408	10	Yes	
NI	30	6756	10(x)	Yes	Broad
NI	29	6955	7	Yes	Film sensitivity down
OI	9	6455	7	Yes	Broad
NI	*	5177	6	Yes	
NI	*	4389	5	Yes	
NI	16	6004	4(x)	Yes	Broad
NI	22	6465	4(x)	Yes	Combined with NI ²¹ above
OI	65	6654	4	?	Under NI ²⁰
NI	31	6723	3(x)	?	Under NI ³⁰
NI	24	5620	3(x)	Yes	Very broad
NI	*	5201	2	Yes	
OI	12	5330	1	Yes	Broad
NI	32	5836	1	Yes	
OI	11	5436	1	Yes	

* Tabulated by NBS⁷, not listed by Moore¹³

(x) Not tabulated by NBS, listed by Moore

et al.¹² as tabulated by Wilson and Nicolet.⁹ The multiplets were listed in order of decreasing multiplet spectral emission coefficient for the reflected shock states of Table A2. A spectral ordering was selected because of its applicability to film exposure (ref. Eq. 5) although this ordering involves the theoretical half-widths which may be uncertain. The ranking of multiplets rather than individual lines was a numerical convenience and can make a multiplet consisting of narrow, widely-spaced lines appear too high on the list. However, the emphasis here was not on a precise ordering but rather for a qualitative list as an aid to identification. While Table 1 was prepared from the listing at $U_s = 6.8 \text{ mm}/\mu\text{sec}$, the ordering did not change much at other conditions and can be considered applicable over the range of conditions shown on Fig. 7. Only multiplet wavelengths in the 2500-7000 Å region were tabulated. Most of the IR lines would lie at or near the top of the list and hence a future effort will be directed toward photographing the IR spectrum.

It is evident from the comments on Table 1 that all the listed multiplets were identified with but three exceptions. Two of these underlie stronger multiplets and hence are questionable while the third - the supposedly prominent multiplet OI^* (6242) - was never seen. While this table is not intended to be a complete listing, it includes most of the prominent multiplets. There are four other multiplets at wavelengths about 4670, 4485, 4435, and 4350 Å that, until recently, defied identification. However a comparison with the spectral scans by Morris et al.¹¹ of a nitrogen arc definitely establishes these to be nitrogen.

There are several mis-identifications on Fig. 7 that have been rectified in Table 1. For example, on Fig. 7, the OI^{10} (3947) ought to be OI^3 , the 4670 Å identification of OI^{17} and OI^{18} is erroneous - the lines are far too narrow (also see above), and the OI^2 identification at 6750 ought to be NI^{30} .

The only impurity lines ever positively identified in emission were those of hydrogen - $\text{H}\alpha$ (6563) was ever-present and prominent and $\text{H}\beta$ (4861) was apparent on most spectrograms. The hydrogen probably came from water vapor

either present on the shock tube walls and not removed by pumping or present in the test gas where it was ineffectively trapped. The shock tube was typically evacuated to below 0.001 torr while the initial pressure was 0.2 torr. The number densities obtained during the $H\alpha$ fitting procedure discussed earlier yielded typical hydrogen concentrations of a small fraction of a percent.

If other impurities were present, their radiative signatures were always buried in the noise level of the film. This was an unexpected result since no claim is made for extreme shock tube cleanliness although the tube was cleaned by dry-wiping between each shot. This result means that the spectrally-integrated radiation was not significantly affected by impurities, at least in the 2500-7000 Å spectral interval.

On one shot the rapid-closing shutter failed to close and the spectrogram was exposed by the entire radiative history of the reflected shock region. The resultant overexposed film revealed a number of absorption lines and the lines of Fe, Cr, Ni, and Al were positively identified. The first three probably came from the stainless steel shock tube walls while the only aluminum known to be in the system was that of the trigger wire in the driver.

Another purpose of the spectral surveys was to locate intervals which were free of line radiation and hence could be used to measure the continuum intensity via the polychromator. Unfortunately, as a scrutiny of Fig. 7 will show, there was no such interval where one could unequivocally state that an intensity measurement was that of only the continuum. Nevertheless, since two extra polychromator channels were available, exit slits were placed near the mercury green line (5460 Å) where one might hope to measure the continuum and at 7032 Å which was a fool's paradise since the film sensitivity (Fig. 4) was too far down to see anything. These two channels are called "continuum?" because about the best that can be said is that they yield an upper bound. Their main function was to provide a basis for

comparison against the continuum intensity levels that were a by-product of the line intensity measurements.

Proof of Steady State

This section is devoted to a demonstration of the temporal behavior of the traces from the photomultiplier tubes in the polychromator and spectrograph (zero-order). The object is to show that the radiation was fairly constant with time and moreover that the behavior of the various spectral features was quite similar.

This latter fact is shown by Fig. 8 which contains traces from an early polychromator configuration where the exit slits were located to obtain the time behavior of six different spectral features - molecular radiation, lines of NI and OI, the continuum?, an impurity line, and the zero-order spectrum. All six traces are remarkably similar in their temporal behavior and this was taken to indicate the presence of chemical equilibrium. The fact that the nonspectral zero-order trace was among these six means that a white-light photomultiplier trace is a valid measure of temporal variations in plasmas of this type. The 30-40% droop began at about 30 μ sec which was the end of spectrograph exposure time. The N_2^+ trace shows a small signal about 10 μ sec prior to the arrival of the reflected shock which corresponds to the passage of the incident shock through the field of view. The traces shown on Fig. 8 are typical of a series of four shots at various shock velocities taken early in the experiment to establish the presence of chemical equilibrium and show that time-integrated spectroscopic recording of film was a valid technique.

To further demonstrate the temporal behavior, various photoelectric traces from twelve recent shots are shown on Fig. 9 where they are arranged in order of increasing incident shock velocity. The traces are principally from either the 5469 A continuum channel of the polychromator or the model profile which was the white-light monitor taken between the energy detectors (see ref. 1 for more details). If neither of these were available, then the zero-order trace of the spectrograph was used - this is less desirable here because the rapid-closing shutter terminates the trace at the end of the exposure time. When

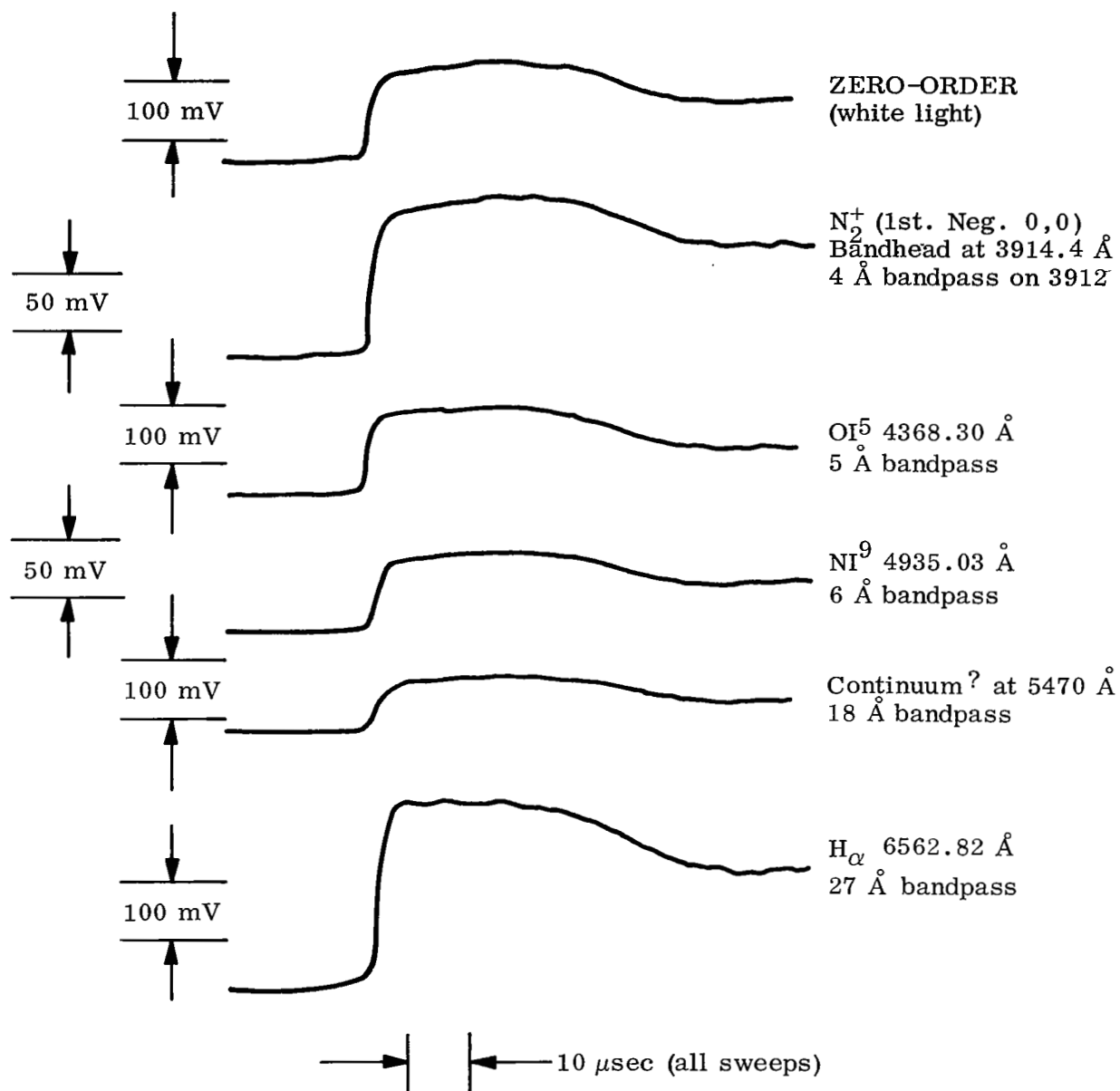
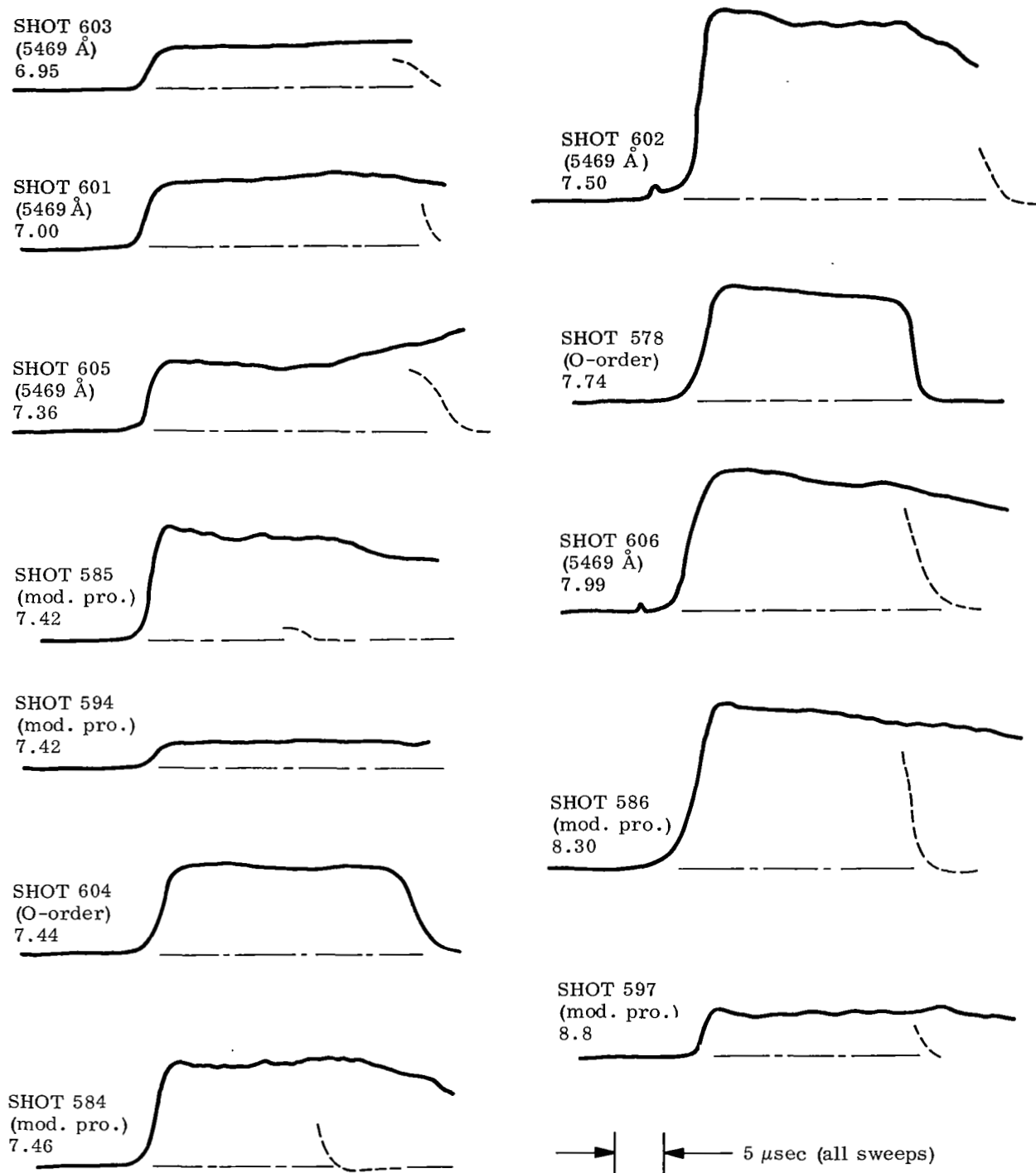


Fig. 8 Photomultiplier Traces from Polychromator on Shot #590
($U_S = 6.85 \text{ mm}/\mu\text{sec}$)



Dashed curves are zero-order traces from spectrograph
Incident shock velocities are in mm/μsec

Fig. 9 Various Photoelectric Traces from Twelve Shots

available, the zero-order traces are superimposed on the others to indicate these times. Because of the similarity between the various photoelectric traces on any one shot, the choice of the particular one used here is unimportant.

Although shot-to-shot variations are clearly apparent on Fig. 9, the broad trend of these traces shows that they are generally flat for $U_s < 7.5$ mm/ μ sec while those at higher incident shock velocities generally show a gradual decrease with time. This may very well have been caused by radiative cooling although, because the radiation is such a sensitive function of temperature, the resultant temperature decrease is quite small. For example, the temperature sensitivity of the visible continuum at 14,000 K ($U_s = 8.3$ mm/ μ sec) is 7.7. Assuming a liberal 15% decrease in the 5469 Å continuum trace over 25 μ sec, the corresponding drop in temperature would be only $15/7.7$ or 2%. Further because the thermometric measurement techniques discussed earlier were both time-integrated to a certain extent, the measured temperatures represent a time-averaged value which would deviate from the original value by about 1%. Considering that the precision of the measurements themselves was about $\pm 4\%$, this variation is insignificant. Thus for the purpose of measuring plasma temperatures, the assumptions of chemical equilibrium and steady state conditions were valid.

The test times behind the incident shock were determined through other photoelectric monitors (see ref. 1) and were generally 20-30 μ sec. For these experiments, the geometry was such that these times are very nearly equal to the times required for a sonic disturbance from the reflected shock-contact surface interaction to propagate into the field of view. These would be minimum values for the reflected shock test times and are compatible with the 25-30 μ sec spectrographic exposure times.

Selection of Plasma Thermometers

On the basis of scans like those of Fig. 7, the various lines and multiplets used to measure the plasma temperature both through shape and intensity measurements were selected.

For intensity measurements, well-known, prominent atomic lines or multiplets were desired. The NI^9 (4935 Å) line and the OI^{10} (6157) and NI^{21} (6490) multiplets were selected since they possessed the fewest disadvantages. The NI^9 (4935) line was bright and narrow, but was located in a spectral region where film sensitivity variations could be important (ref. Fig. 4). The prominence of the OI^{10} (6157) overshadowed its asymmetry and red shift. The NI^{21} (6490) multiplet was not always prominent and is not listed by NBS,⁷ but it was close to $\text{H}\alpha$ where an absolute intensity was needed and it was tabulated by Wilson and Nicolet.⁹ In retrospect the NI^{20} (6644) multiplet might have been a better choice since it was listed by NBS, but NI^{21} was somewhat more easily separated from other lines. The polychromator exit slit widths were selected to be about six times the line or multiplet half half-width at nominal conditions and are tabulated below. The wavelengths are those of the centerlines and $\Delta\lambda$ is the full width of each exit slit.

<u>Spectral feature</u>	<u>λ, Å</u>	<u>$\Delta\lambda$, Å</u>
NI^9	4935	4.6
Continuum?	5469	16.6
OI^{10}	6163	45.8
NI^{21}	6488	47.1
Continuum?	7032	16.7

For shapes, the candidate had to be a single line in addition to being well-known and prominent. NI^9 (4935) met this added restriction and $\text{H}\alpha$ (6563) was considered well-known despite the shape controversy mentioned earlier. The better-known $\text{H}\beta$ (4861) was not prominent and could only be used on one shot when an unusually high (1.3%) hydrogen concentration made it usable.

RESULTS

The results of the plasma temperature measurements are presented and discussed in this chapter. They were obtained on the six shots for which both spectrographic and polychromatic results were available. These shots had incident shock velocities in the range of 7-8 mm/ μ sec and yielded average measured temperatures from 10,750 to 13,000 K. Examples of the techniques and interesting qualitative results will be presented first.

Examples of Shape-Fitting

In this section are presented examples of the shape-fitting process taken from these six shots. The lines considered were the 4935 Å line of Ni^9 , $\text{H}\alpha$ (6563 Å) and, on one occasion, $\text{H}\beta$ (4861 Å). The criterion used to determine the best fit between the computer-generated shape and the experimental profile was that the fit criterion δe be a minimum where:

$$\delta e = \frac{1}{\sqrt{N}} \left[\sum_{i=1}^N [e(\lambda_i)_{\text{expt.}} - e(\lambda_i)_{\text{theor.}}]^2 \right]^{1/2} \quad (37)$$

Here $e(\lambda_i)$ refers to the experimental and theoretical relative exposure values at a wavelength λ_i . The minimum value of the fit criterion is shown on the examples which follow.

Figure 10 shows the measured profile and the best-fit theoretical data points for $\text{H}\alpha$ on one of the slower incident shock velocities using the shape taken from Griem.¹⁰ The minimum value $\delta e = 0.033$ was higher than most for this experiment. The fit using the Morris et al.¹¹ correction to the Griem half half-width (the width at every point was changed by this amount) would be similar but the resultant electron density would be lower. The results for Ni^9 on this same shot are given in Fig. 11 which also contains the instrument function to indicate that it must be included in the data reduction procedure for shape measurements on narrow lines. As indicated by the value $\delta e = 0.011$ the theoretical points fit the measured profile quite well.

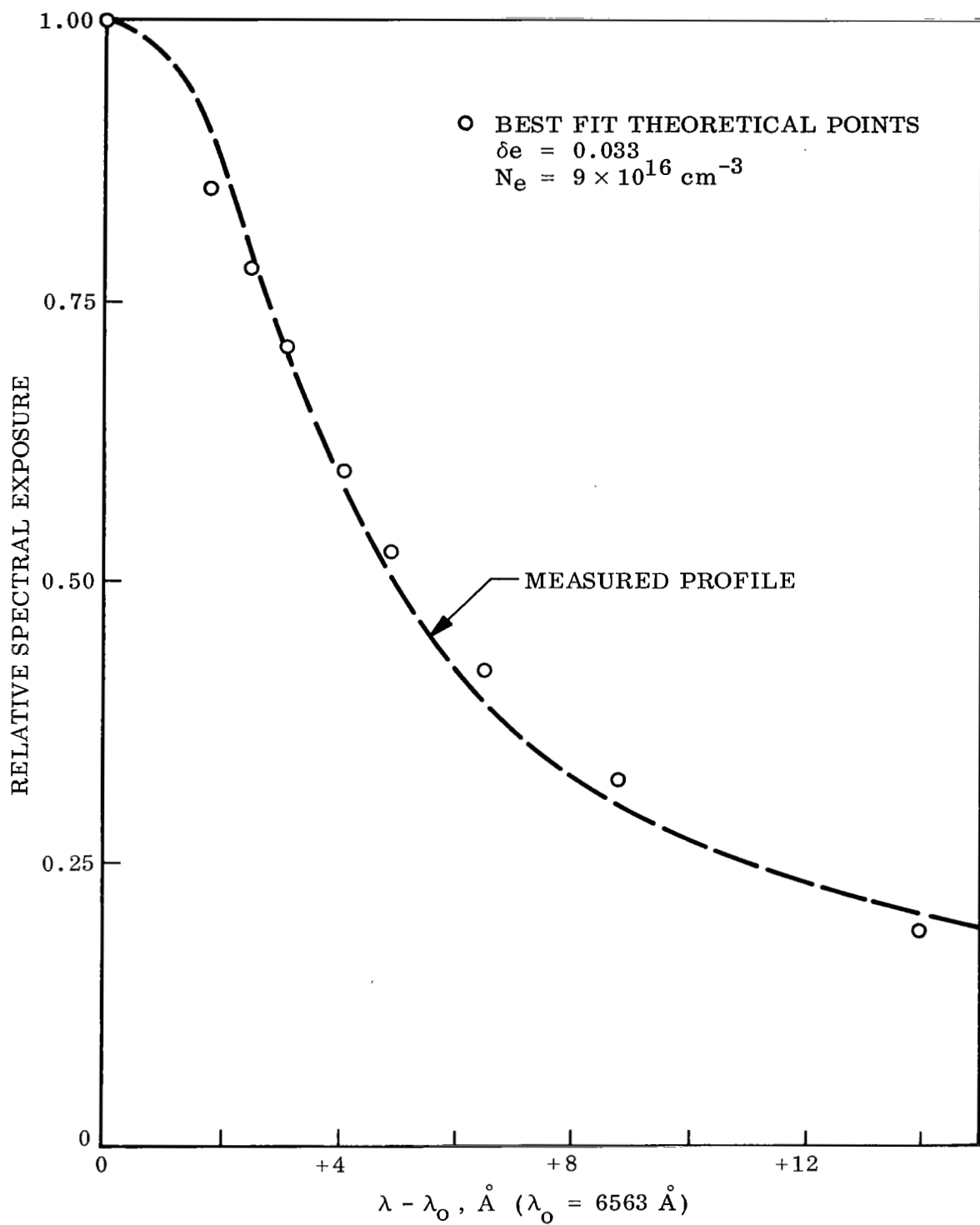


Fig. 10 Example of Shape-Fitting Process for $H\alpha$ on Shot #601
 $(U_S = 7.00 \text{ mm}/\mu\text{sec})$

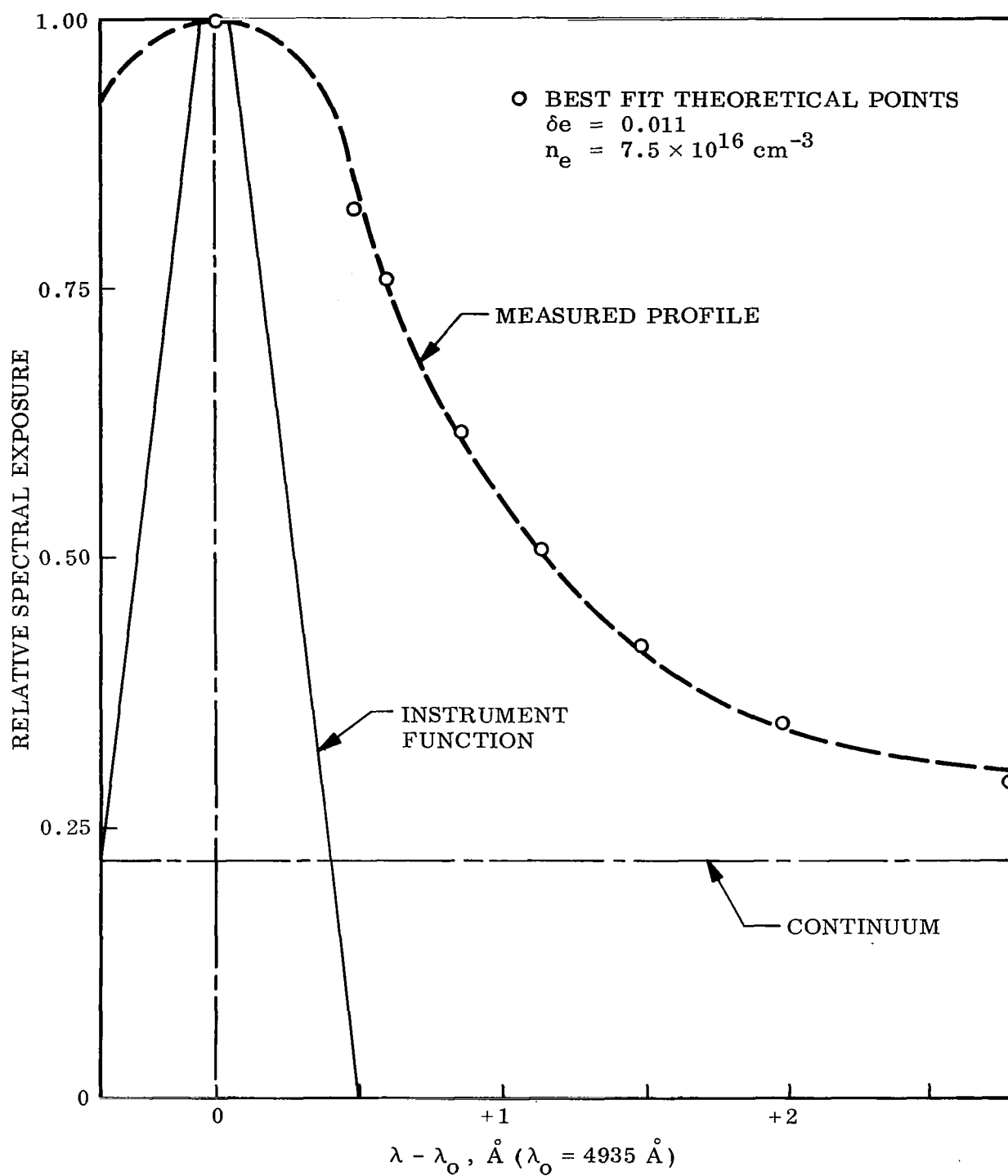


Fig. 11 Example of Shape-Fitting Process for NI^9 on Shot #601
 $(U_S = 7.00 \text{ mm}/\mu\text{sec})$

Following this shot (which was the first of the six) it was decided to fit the entire profile rather than just half. To fully utilize the features inherent in the RMS fit criterion (Eq. 37), the measured profiles were read directly into the computer as taken from the microdensitometer traces even though these profiles contained obvious noise. An example of a noisy profile is shown by Fig. 12 for NI^9 at an intermediate shock velocity. Here the value $\delta e = 0.039$ was rather high which was to be expected from the nature of the measured profile, but the resultant electron density yielded a temperature in good agreement with the other measurements as will be shown later. The exit slit width of the polychromator $\Delta\lambda$ is shown in this figure for informative purposes only - the polychromatic result was not used in the fitting process for NI^9 and only in a relatively unimportant way for $\text{H}\alpha$.

The NI^9 profile for the highest incident shock velocity of these six shots is shown by Fig. 13 which also indicates the rapid rise of the underlying continuum. The attendant high electron density broadened the line to the point where the wing of the 4915 Å line in the NI^9 multiplet overlapped noticeably. This overlapping was accounted for (approximately) by lowering the profile on the blue wing as shown. Another and probably better approach would be to fit both lines of the NI^9 multiplet simultaneously. This technique would be applicable here because there are no other adjacent lines to cause difficulty (NI^9 is singular in this respect). Even though the continuum level was relatively high, the fit was quite good as indicated by the low value of the fit criterion ($\delta e = 0.006$). These last three figures also indicate that NI^9 does indeed have a Lorentzian line shape.

As mentioned earlier, $\text{H}\beta$ was often only barely discernable above the continuum. This happens because it is inherently a weaker line than $\text{H}\alpha$ (the maximum absorption coefficient is 1/30 of that for $\text{H}\alpha$) and is located in a region where the air continuum is higher. However, on one shot the H_2 concentration was abnormally high ($\sim 1.3\%$) and $\text{H}\beta$ stood well above the continuum. This profile and the results of the shape-fitting process are shown on Fig. 14. The calculations were done by hand using the shape given by

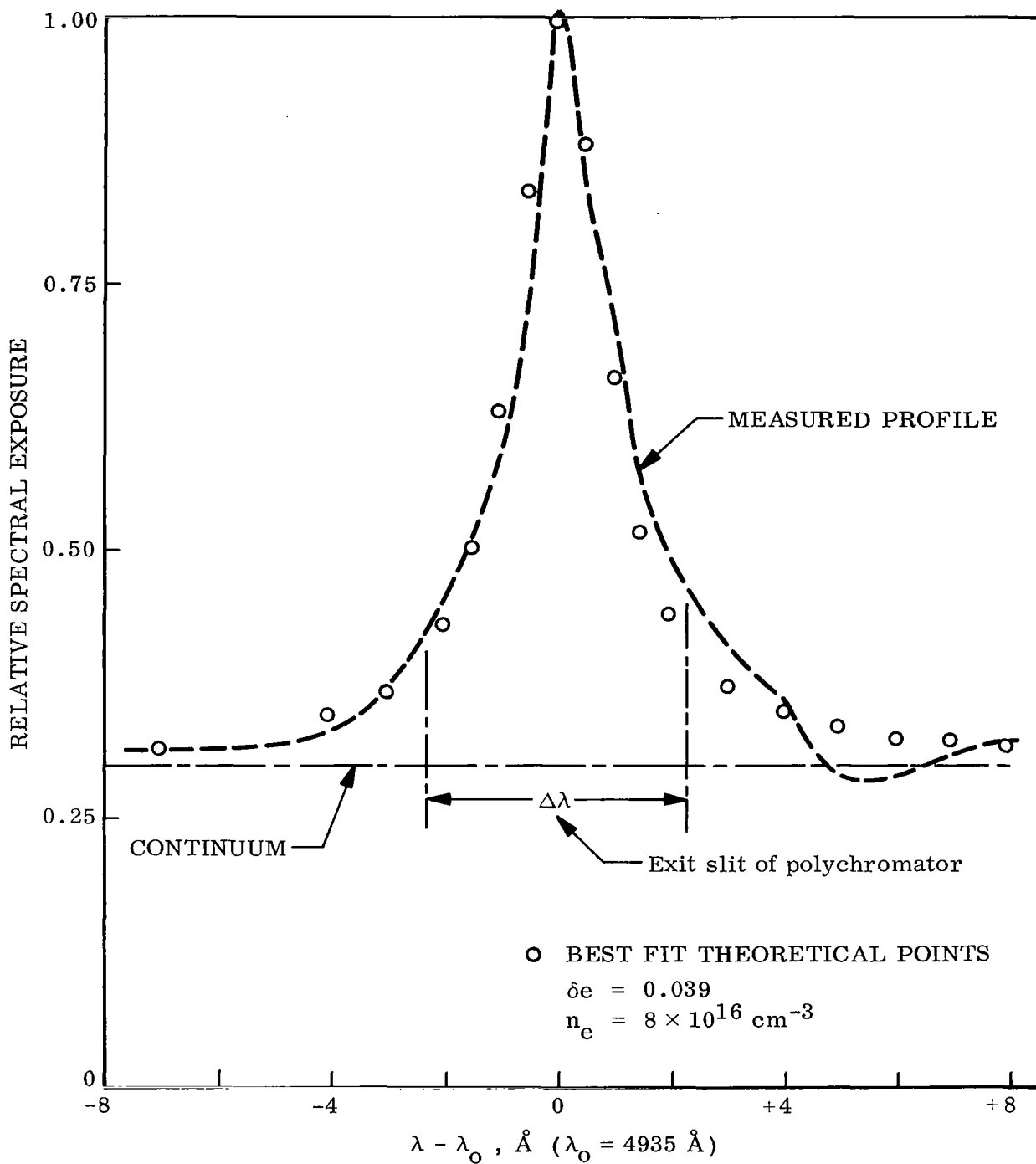


Fig. 12 Example of Shape-Fitting Process for NI^9 on Shot #605
 $(U_S = 7.36 \text{ mm}/\mu\text{sec})$

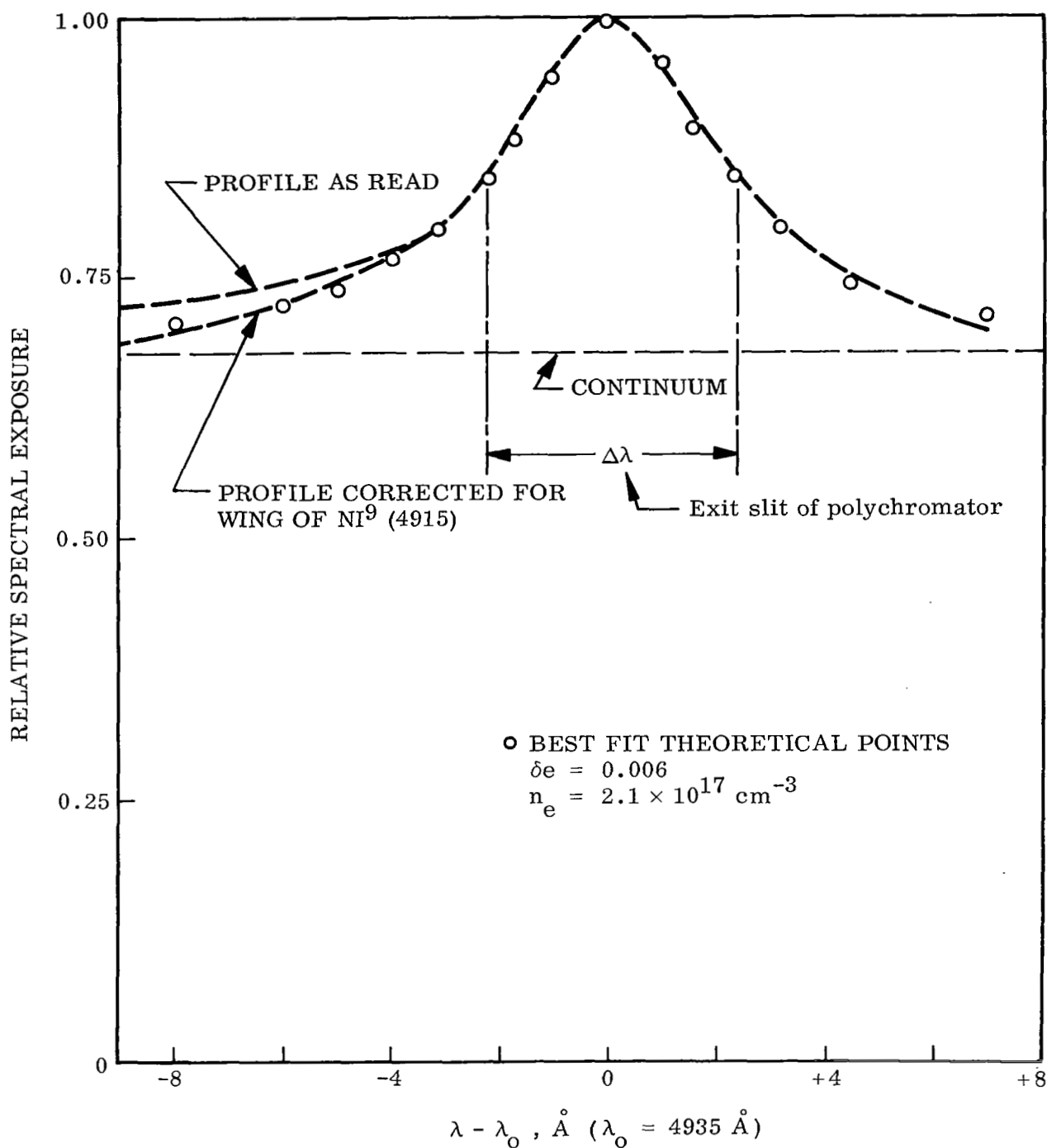


Fig. 13 Example of Shape-Fitting Process for NI^9 on Shot #606
 $(U_S = 7.99 \text{ mm}/\mu\text{sec})$

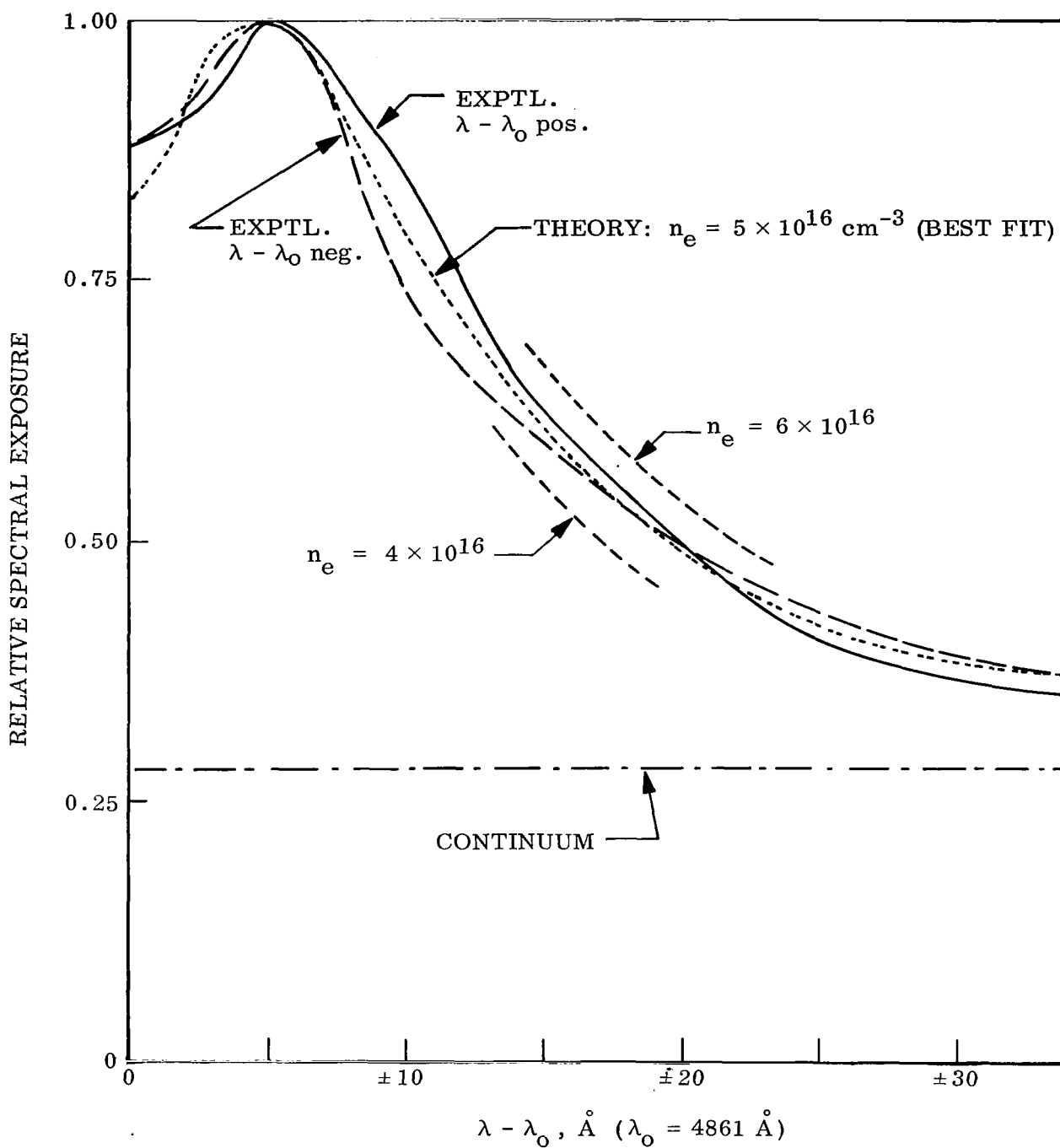


Fig. 14 Results of Fitting a Shape to HB Profile on Shot #603
($U_S = 6.95 \text{ mm}/\mu\text{sec}$)

Griem¹⁰ and the effects of the instrument function and opacity were neglected. The abscissa of Fig. 14 indicates that the instrument function was relatively quite narrow while an intensity calculation revealed that the peak emissivity was about 0.10 so opacity effects were small.

This figure shows that the best fit profile corresponded to an electron density of $5 \times 10^{16} \text{ cm}^{-3}$. Portions of the shapes for electron densities perturbed by $\pm 20\%$ are shown to indicate the sensitivity of the fit. H β is a well-studied line whose shape is reported by Griem¹⁰ to be good to 3% for $n_e = 3 \times 10^{16} - 3 \times 10^{17} \text{ cm}^{-3}$ and $T = 10\text{-}20,000 \text{ K}$. Because of this low uncertainty on the theoretical shape, an error analysis similar to that done earlier indicates that H β was a $\pm 2\%$ thermometer on this shot. This suggests another possible thermometric technique that will be further discussed later.

The reason why the H α and H β shapes cannot be used simultaneously is typified by this shot. The relative exposure profiles for NI²¹ and H α revealed that the H α peak intensity was 3.7 times that of the fairly-bright NI²¹ multiplet. Scaling up the polychromatic result gave an emissivity very near unity. With this high opacity, the shape-fitting process becomes far too dependent on an intensity measurement, e.g. lowering the H α peak intensity by 20% doubled the resultant best-fit electron density. This is obviously an unsatisfactory situation and hence the H α shape was essentially useless on this shot. This effect could be mitigated by shortening the pathlength and later this approach will be further discussed. However, for the 30.5 cm pathlengths of this experiment, it was impossible to measure both H α and H β simultaneously under conditions where the shape-fitting process was meaningful for both lines.

Examples of Line Overlap

Figure 13 revealed that a small overlap occurred between the lines of NI⁹ at the higher electron densities. While this did not cause much difficulty on NI⁹, line overlap seriously limited the usefulness of the polychromatic results

for NI^{21} and OI^{10} . This is illustrated by Fig. 15 which contains the relative exposure profiles for the 6410-6570 Å region for three shots - an intermediate and the two extremes of incident shock velocity. This spectral region contains one OI and three NI multiplets and $\text{H}\alpha$. The wavelengths for these are indicated at the bottom of the figure as is the position and width of the appropriate polychromator exit slit. By superposing the three profiles, the effects of line broadening, shifting, and overlapping and the rising of the continuum become most apparent.

It is evident that only OI^9 , NI^{21} , and $\text{H}\alpha$ are the important radiators in this region, but despite this simplification it becomes increasingly difficult to separate the contributions from these three multiplets at the higher incident shock velocities. In fact, no attempt was made to separate them on the upper profile (shot 606) because the errors on the resultant temperature obtained from the NI^{21} integrated intensity would be unreasonably large. This typifies the difficulties encountered in attempting to measure the intensity of a line or multiplet that is not well isolated. Figure 15 also typifies the difficulties in attempting to fit the shape of $\text{H}\alpha$ since the profile is strongly influenced by the overlap from NI^{21} (and from NI^{20} on the red side of $\text{H}\alpha$).

Examples of Combined Results

Examples of the combined results from the polychromator and the spectrograph are given by the following three figures (Figs. 16-18) which again represent an intermediate and the extremes of incident shock velocity. The solid symbols on these figures represent the polychromatic results (ref. Eq. 10) for the three line and two continuum measurements using the exit slits tabulated on p. 52. As discussed earlier, these solid symbols represent a spectral intensity averaged over the spectral width of the exit slit.

For each of the three polychromatic measurements which included a line or multiplet, combination with the relative exposure profile from the spectrograph yielded a peak spectral intensity (Eq. 12) if the effect of the instrument

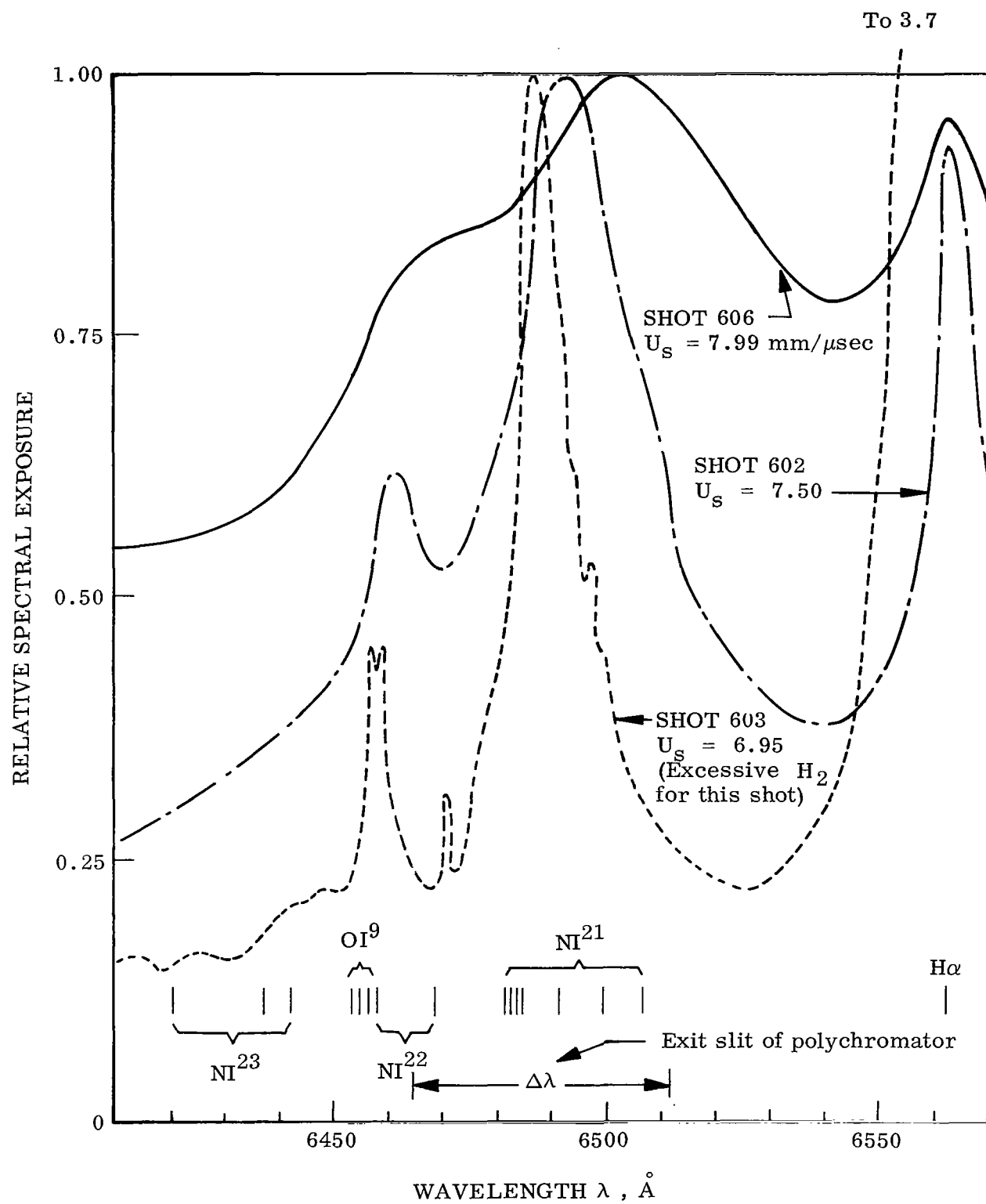


Fig. 15 Profile Extremes About NI²¹

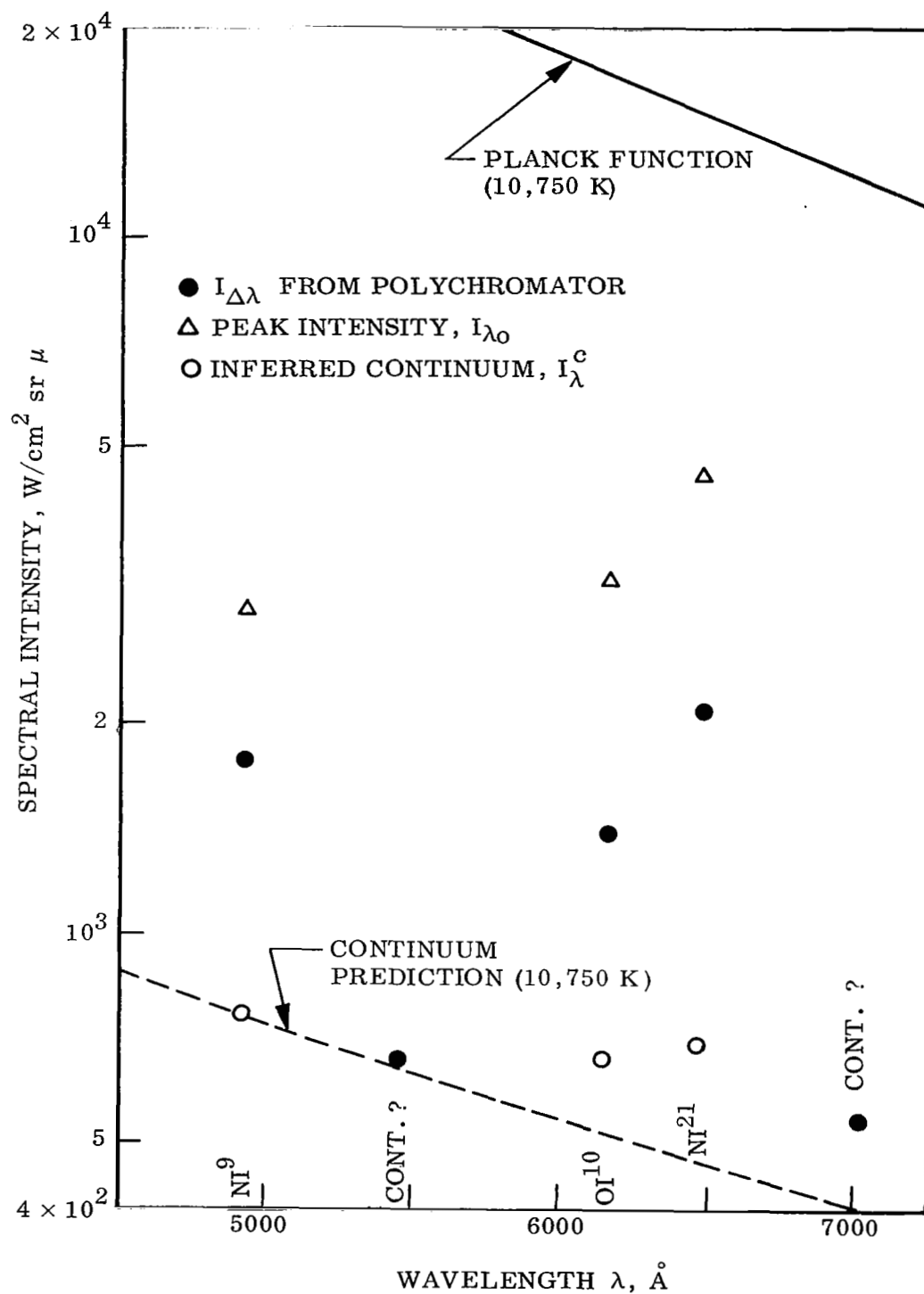


Fig. 16 Combined Results for Shot #603 ($U_s = 6.95 \text{ mm}/\mu\text{sec}$)

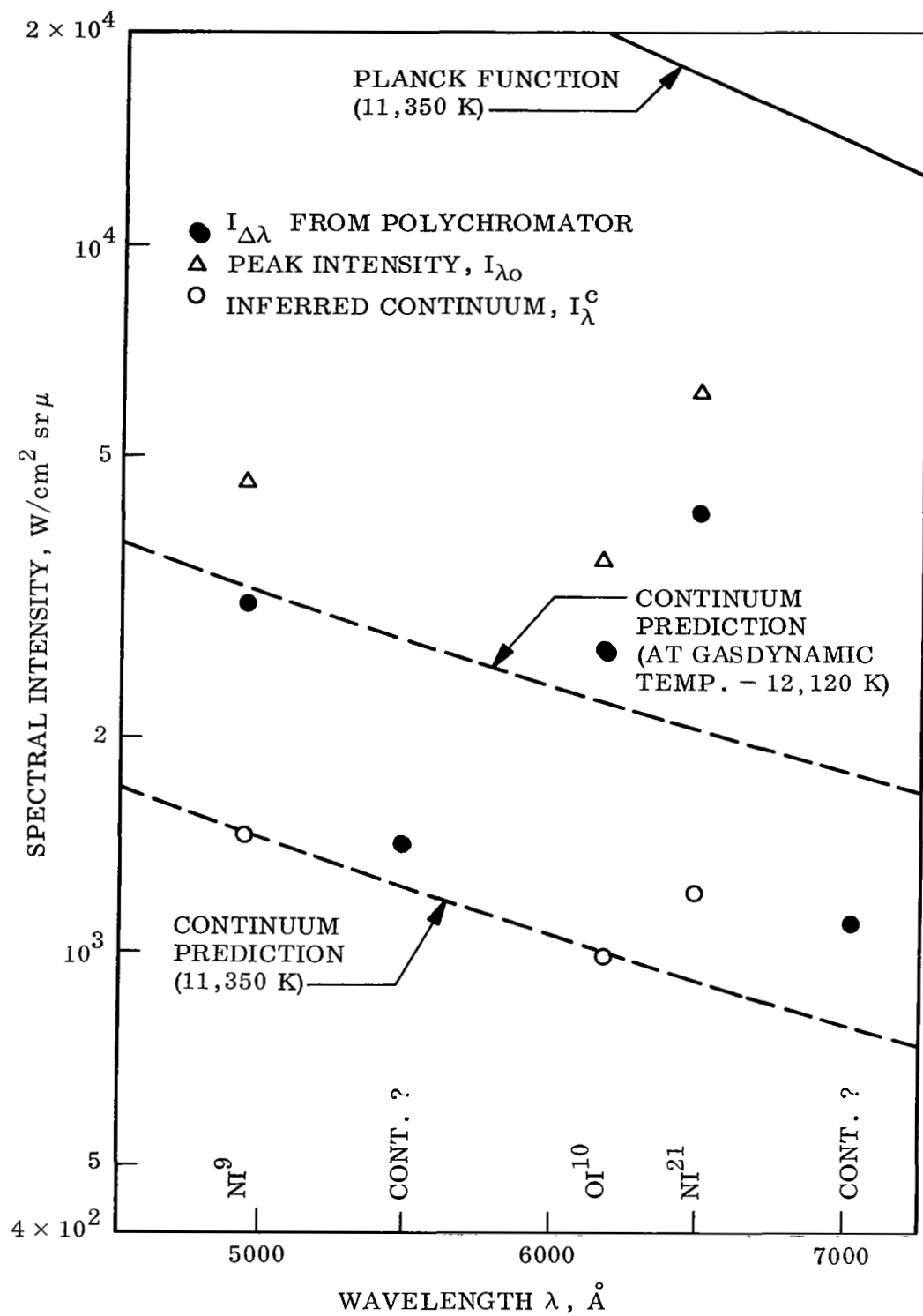


Fig. 17 Combined Results for Shot #605 ($U_s = 7.36 \text{ mm}/\mu\text{sec}$)

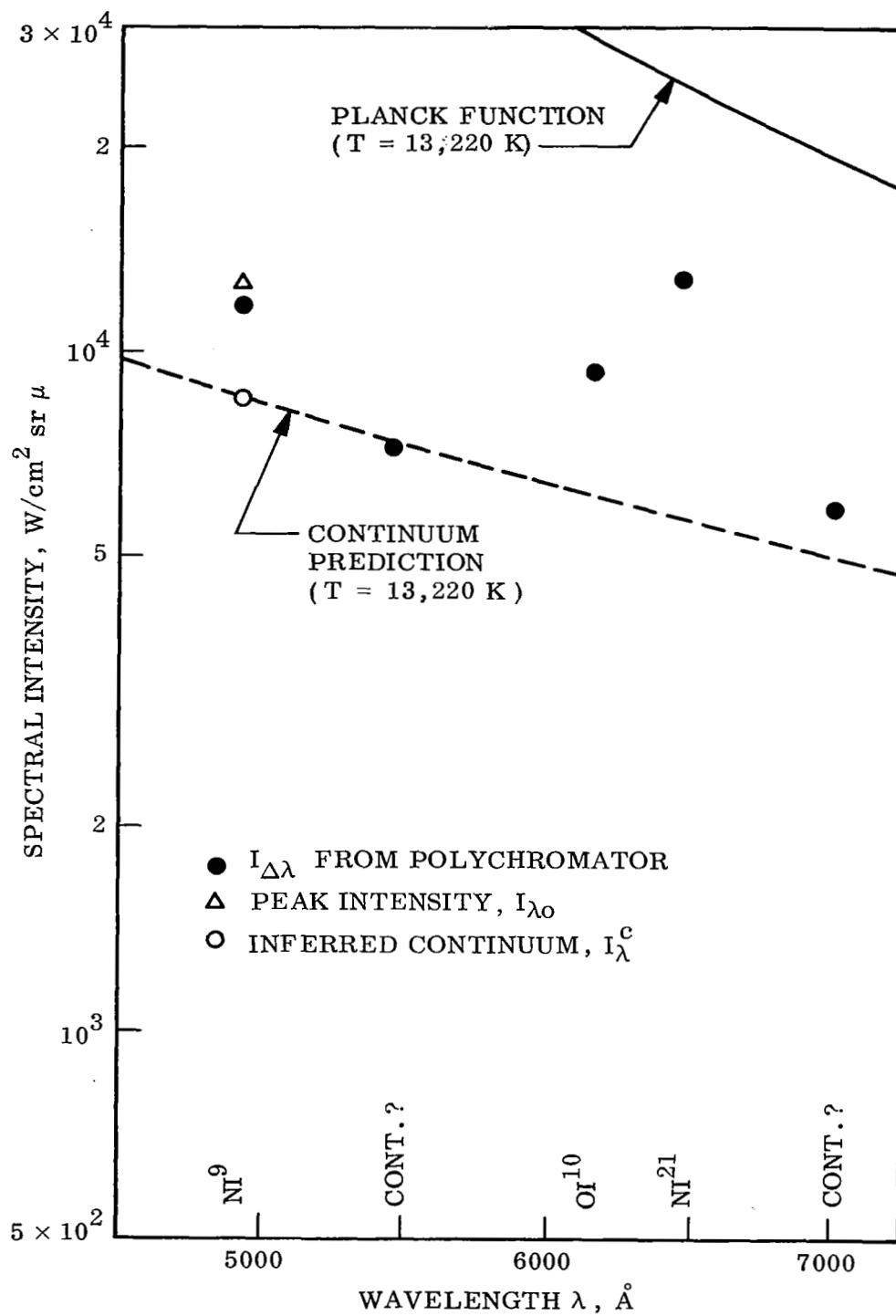


Fig. 18 Combined Results for Shot #606 ($U_s = 7.99 \text{ mm}/\mu\text{sec}$)

function was neglected. Also the shape-fitting process yielded a value for the continuum level (ref. p. 38). Both of these values are indicated by the open symbols on Figs. 16-18 and represent true spectral intensities.

The main purpose of these plots was to provide a graphical comparison between the inferred continuum level from the three line intensity measurements and the two direct measurements of the continuum. This provided a consistency check and on one occasion uncovered an error in the microdensitometric process. For reasons discussed in the next section, the continuum prediction was fit on the 4935 Å continuum intensity and the resultant curves are shown. These curves were generated from a smeared continuum model where the photoionization edges are lumped and hence detailed spectral features disappear. Hence little more can be said about this curve except that the other continuum points lie quite close or slightly above it. The important fact is that these points showed consistency from shot to shot.

The Planck function, evaluated at the temperatures associated with the continuum predictions, is also shown on these three figures. It is noted that the Planck function changes relatively slowly with temperature. The much more rapid rise of the continuum and the attendant approach to the Planck function is shown quantitatively by these three figures. On Fig. 18, the Ni^9 peak emissivity was 0.29 while the Ni^{21} value was about 0.5. Obviously, these peak emissivities can be reduced by shortening the pathlength.

However of much more importance to the validity of the temperature measurements is the fact that the continuum intensity is approaching or even exceeding the peak intensities of the lines. This is demonstrated by mentally picturing where a curve of twice the continuum prediction would fall on Fig. 18. Now since the polychromatic measurement includes contributions from both the lines and the continuum, high continuum levels mean that the line intensity is becoming the difference between two large numbers. As pointed out in the error analysis, this leads to large uncertainties in the integrated line intensity and hence large errors in the resultant plasma

temperature. It is the rapidly-rising continuum, and not the increased opacity, that limited the usefulness of this thermometric technique.

The Thermometric Use of the Continuum

A possible thermometric technique that has not been discussed as yet involves the continuum itself. This is basically attractive because of a high temperature sensitivity of the continuum and it is this that has made the line measurements increasingly unattractive. However, the theoretical continuum cross sections are generally quite uncertain and limit the usefulness of such a thermometer.

But Morris et al.¹⁴ have extensively studied the continuum of nitrogen at 4955 Å and recommend that their values of absolute intensity be used to determine a plasma temperature. Accordingly, the values for the spectral continuum intensity of air at 4955 Å taken from the theoretical predictions (see ref. 1) which used a smeared continuum model were compared against the detailed results of Morris et al.¹⁴ for nitrogen at corresponding temperatures and pressures. The agreement was remarkable (and very probably fortuitous). The predictions were about 10% high in the 10,500-12,000 K range (which is to be expected when comparing air to nitrogen) and essentially in agreement in the 13,000-14,000 K range of reflected shock conditions.

The result of the integrated intensity measurement and shape-fitting process on NI⁹ (4935 Å) gave, as a byproduct, a value for the continuum spectral intensity. Also the continuum predictions, when fit on these values, were consistent with the other four continuum measurements as shown by Figs. 16-18 and thus increased our confidence in these 4935 Å values. Thus because good experimental values for the 4935 Å continuum spectral intensities were available and because the predictions were essentially in agreement with the careful experimental studies of Morris et al.,¹⁴ it was decided to evaluate a plasma temperature based on these predictions. The results will be discussed in the next section.

Although placing an exit slit over a line is admittedly not an optimum way to obtain the continuum intensity, this thermometric technique was applied a posteriori and improvements in technique for future measurements could obviously be made. The large temperature sensitivity inherent in this method is demonstrated by the large difference between the two continuum predictions placed on Fig. 17.

Results of the Plasma Temperature Measurements

The culmination of the spectroscopic effort is represented by Fig. 19 which shows the results of the various plasma temperature measurements plotted against the gasdynamic value obtained from the incident shock velocity and initial pressure (ref. Table A2). To aid in the assessment of the data scatter, $\pm 4\%$ error bars were drawn about the line representing temperature equality. These bars represent a reasonable estimate of the experimental errors for the temperature range shown and, with the exception of shot 602, the scatter between all the results on any one shot lie within the heights represented by these bars.

The important conclusions to be drawn from this figure are first that the measured temperatures do not cluster about the gasdynamic value as would be expected if the gasdynamic temperatures were representative of the state of gas and if the measurement errors were randomly distributed. Also some erratic behavior is indicated - e.g. the mean of the measurements on shots 601 and 605 are nearly the same while the gasdynamic values differ by almost 1,000 K. This erratic behavior also suggests that the gasdynamic value does not adequately define the state of the test gas.

Figure 19 contains all the results that could be derived from the six shots for which both polychromatic and spectrographic results were available. Since for each shot there were 3 line intensity measurements (NI^9 , OI^{10} , NI^{21}) and 2 shape measurements (NI^9 and $\text{H}\alpha$), this should yield 30 data points. In actuality there were only 22. The lost points were caused by a misaligned exit slit (1), a bad spot in the negative caused by faulty

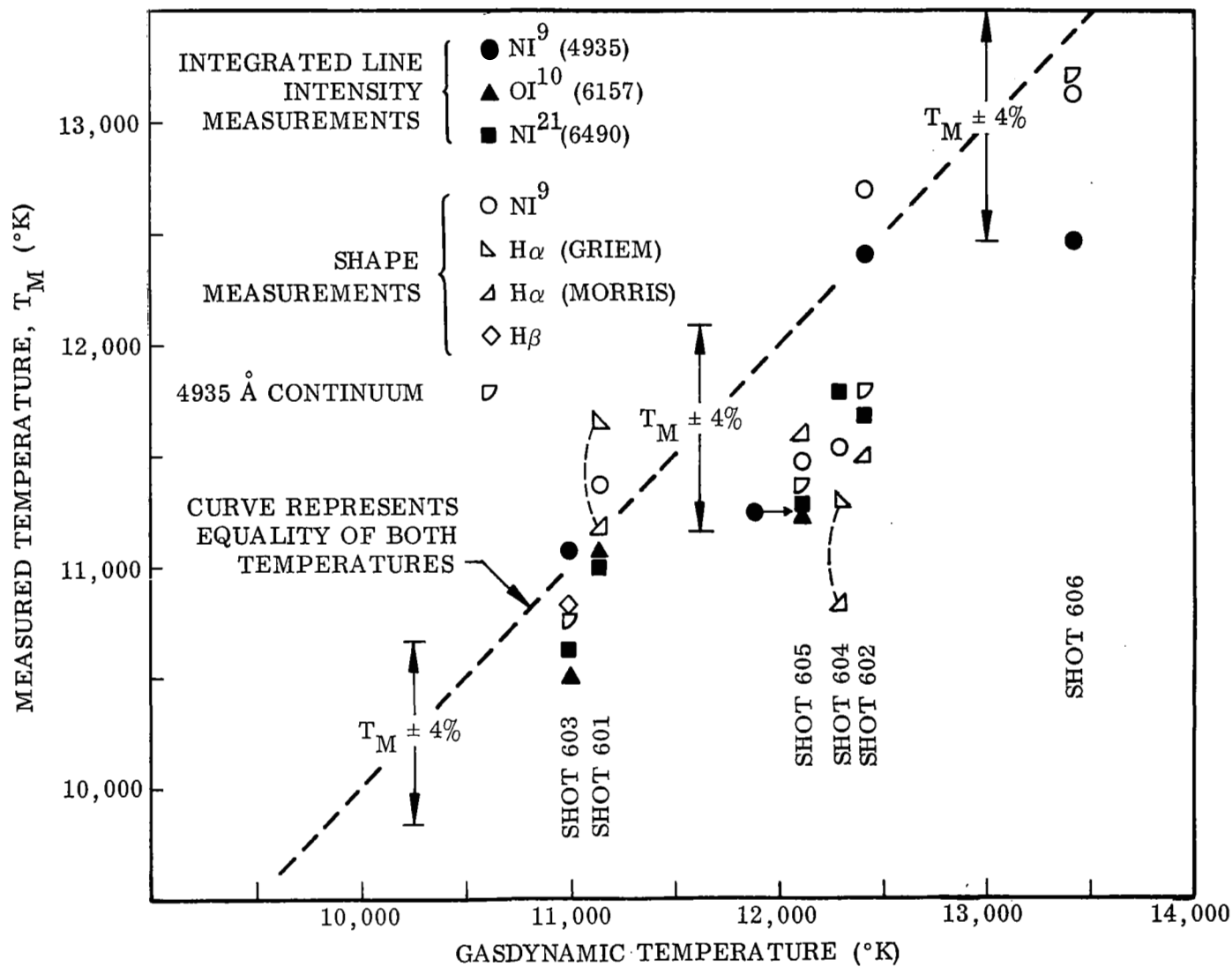


Fig. 19 Results of Temperature Measurements

development (1), off-scale polychromator traces (3) caused by an unexpectedly hot shot, and the inability to utilize the NI^{21} , $\text{H}\alpha$, and OI^{10} data on shot 606 because of the high continuum level (ref. Fig. 15).

On shot 603, the unusually-high hydrogen concentration made $\text{H}\alpha$ unusable but this in turn yielded a good profile for $\text{H}\beta$ (ref. Fig. 14) which, as discussed earlier, was a 2% thermometer. The resultant temperature is gratifyingly close to the mean of the other measurements. Also the NI^9 intensity measurements made possible the continuum thermometer discussed earlier. These points are included on Fig. 19 and also lie quite near the mean of the measurements. Note also the good correspondence between the $\text{H}\beta$ and the 4935 A continuum results on shot 603.

The above statements are clarified by Fig. 20 which compares the deviation of the various measurements from the arithmetic mean of all the results (including the 4935 A continuum but excluding the gasdynamic value) available on each shot. The $\text{H}\beta$ value and the four 4935 A continuum measurements lie quite close to the mean value. It is interesting to note that the scatter of the NI^9 integrated line intensity measurements is about twice that of the 4935 A continuum. This must be explained at least in part by a higher temperature uncertainty for the continuum measurements since both absolute intensities were obtained from the same polychromatic result.

Another reason for preparing Fig. 20 was to locate possible one-sided deviations which would point to a systematic error. None is clearly apparent although the OI^{10} and NI^{21} measurements do appear slightly below the mean while the NI^9 shapes all lie above the mean. These however are within the expected errors from uncertainties in the respective f-numbers and half half-widths.

More important is the last column of Fig. 20 which shows the deviations of the gasdynamic values of the plasma temperature. These are definitely one-sided and average about 4% above the mean of the measured temperatures. This

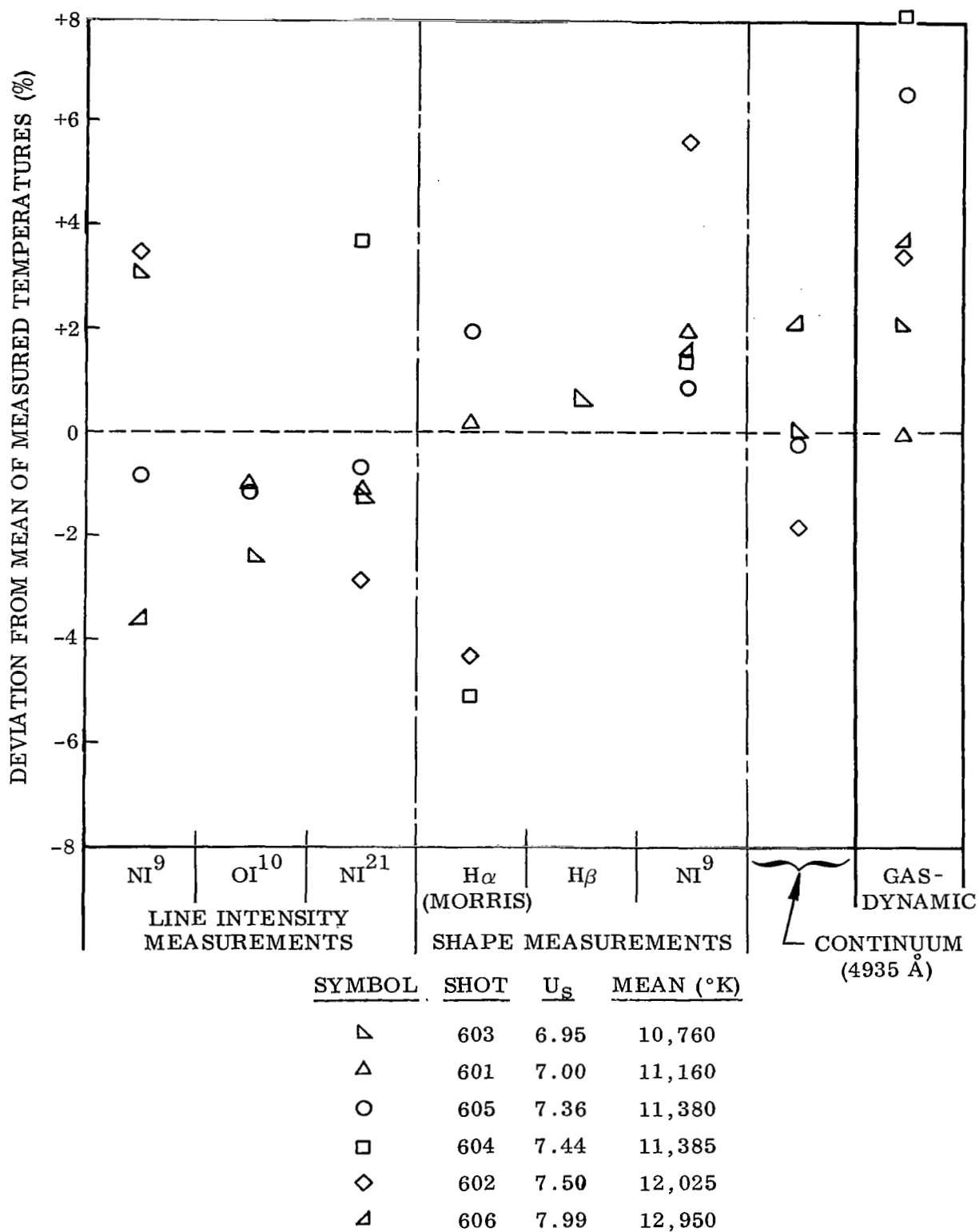


Fig. 20 Comparison of the Results from the Various Thermometric Techniques

is a significant deviation and indicates that the actual reflected shock temperature was somewhat below the gasdynamic value. The erratic behavior of the gasdynamic value is exemplified by the fact that there is no correspondence between the magnitude of the deviation and the incident shock velocity.

All the $H\alpha$ results on Fig. 20 and most of those on Fig. 19 were obtained using the shapes recommended by Morris et al.¹¹ As shown on Fig. 19, the use of the Griem¹⁰ shape would raise the measured temperatures about 4%. As indicated by Fig. 20, the results using the Morris shapes were not sufficiently one-sided to make one shape a clear choice over the other. In fact, to center the $H\alpha$ temperatures about the zero deviation line would require an intermediate shape about halfway between the two.*

* The intermediate shapes recently computed by Kepple and Griem meet this requirement and probably should be used in the future. The reference is Kepple, Paul C., "Improved Stark Profile Calculations for the First Four Members of the Hydrogen Lyman and Balmer Series," University of Maryland Tech. Report #831, 1968.

CONCLUSIONS AND RECOMMENDATIONS

The measured temperatures of this experiment are in reasonable agreement with each other within the limitations imposed by the expected errors. However the mean of these measured values lies about 4% below the gasdynamic temperature. Further, although the number of shots is not as high nor the scatter on any one shot as low as desired, there are indications that the actual temperatures may be randomly scattered in a manner not predictable from the incident shock velocity.

To place the results of this experiment in the proper perspective, recall that the temperatures were measured to shed light on the deviations between experiment and theory for total radiation measurements. At 12,000 K, which is representative of the measurements described herein, the theoretical total radiant intensity predictions lie above the experimental results by a factor of about 1.5 (ref. Fig. A1). Since here the total intensity varies as the tenth power of temperature, this factor of 1.5 could be explained by a 4% temperature difference.

Thus the average 4% difference observed between the measured and the gasdynamic temperatures is certainly in the right direction and of about the correct magnitude to explain the deviation between theory and the experimental total radiation measurements. However it is difficult if not impossible to justify any stronger conclusions on the basis of six \pm 4% measurements when a 4% effect is all-important.

The temperature measurements reported herein were not significantly affected by radiative cooling phenomena. The analysis on p. 53, which was based on actual photoelectric traces obtained at temperatures higher than those measured herein, showed that cooling effects were less than 1%.

In this experiment, temperatures were only measured to 13,000 K which fell short of the desired goal of 16,000 K. The combination of the following two effects limited this range:

1. The rapid rise of the continuum made it difficult to perform adequately precise measurements of the radiative quantities.
2. The temperature sensitivity of the various thermometric techniques decreased sharply.

Thus in short it rapidly became more difficult to make even less-precise measurements.

Nevertheless it is recommended that additional temperature measurements be made and further that these be as precise as possible. Clearly this will require a preliminary analytical effort. However experience in these matters has been gained and the chapter on plasma thermometry outlines a systematic method of approaching the problem. The following thoughts ought to be kept in mind:

1. At the higher temperatures, radiative cooling effects may become important and hence not all the techniques should require that the plasma be in a steady state. (A direct, photoelectric measurement of the 4955 Å continuum is a possibility here.)
2. The plasma could be seeded with another specie which would offer attractive advantages (e.g. the shape of $H\beta$).

Also the existing experimental techniques should be improved to include a measurement of the plasma pressure and the use of a step wedge with finer steps to yield more points on the H-D curve at higher relative exposure levels. In addition the pathlength should be shortened to minimize opacity effects and all spectroscopic apparatus should then be located on the same side of the shock tube.

This report is concluded with a brief comment about the ramifications that these improved and extended property measurements would have on the measurements of the total radiant intensity. The erratic behavior of the gasdynamic

temperature encountered during this research strongly suggests that plasma property and total intensity measurements will have to be performed simultaneously. While this would require an additional effort, the present cavity gage configuration (see ref. 1) was designed for simultaneous measurements and the THT gages are proven and reliable energy detectors. Thus this task would not require an inordinate amount of time and would do much toward validating the current state-of-the-art predictions for the radiant intensity of high-temperature air.

APPENDIX

This appendix contains two figures and two tables included to supplement the discussion in the main text.

The figures present the salient results of the latest spectrally-integrated radiant intensity measurements taken using energy detectors on both this and prior NASA contractual efforts. This work is described in ref. 1. Figure A1 presents the experimental results and a theoretical prediction for the total (i.e. windowless) radiant intensity of air while Fig. A2 presents the results and a prediction for the radiation transmitted by a quartz window.

Table A1 contains numerical values for the total radiant intensity prediction at the conditions of this experiment. These predictions are felt to be representative of the current state-of-the-art. The origin of these predictions is given in ref. 1. It is noted that the values in the first column (line, $< 2,000 \text{ \AA}$) do not always vary smoothly with pathlength. These irregularities were caused by switching from an analytic expression to an exact numerical frequency integration for the equivalent width of certain line groups after the lines had become strongly overlapped. This caused 10% errors in the first column and, of course, much lesser ones in the total intensity column.

Finally Table A2 contains a listing of the thermodynamic states and the species composition in the reflected shock region as computed from the Rankine-Hugoniot equations and an IMSC thermochemical equilibrium program. The data from this table were used to prepare the theoretical predictions shown on Figs. A1 and A2 and certain parts were used in the plasma thermometry discussed in the main text of this report.

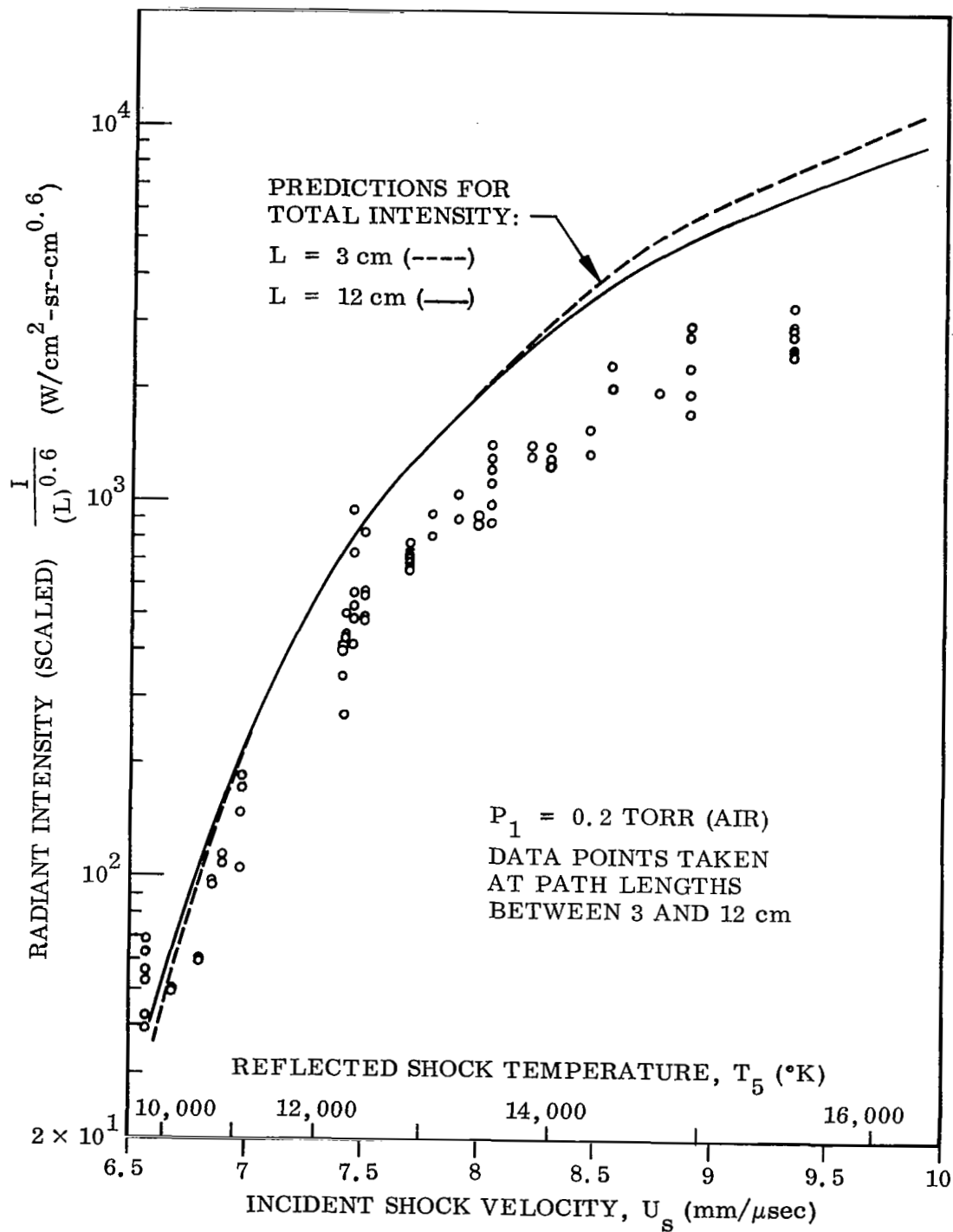


Fig. A1 Experimental Results and Theoretical Predictions for the Total Radiant Intensity.

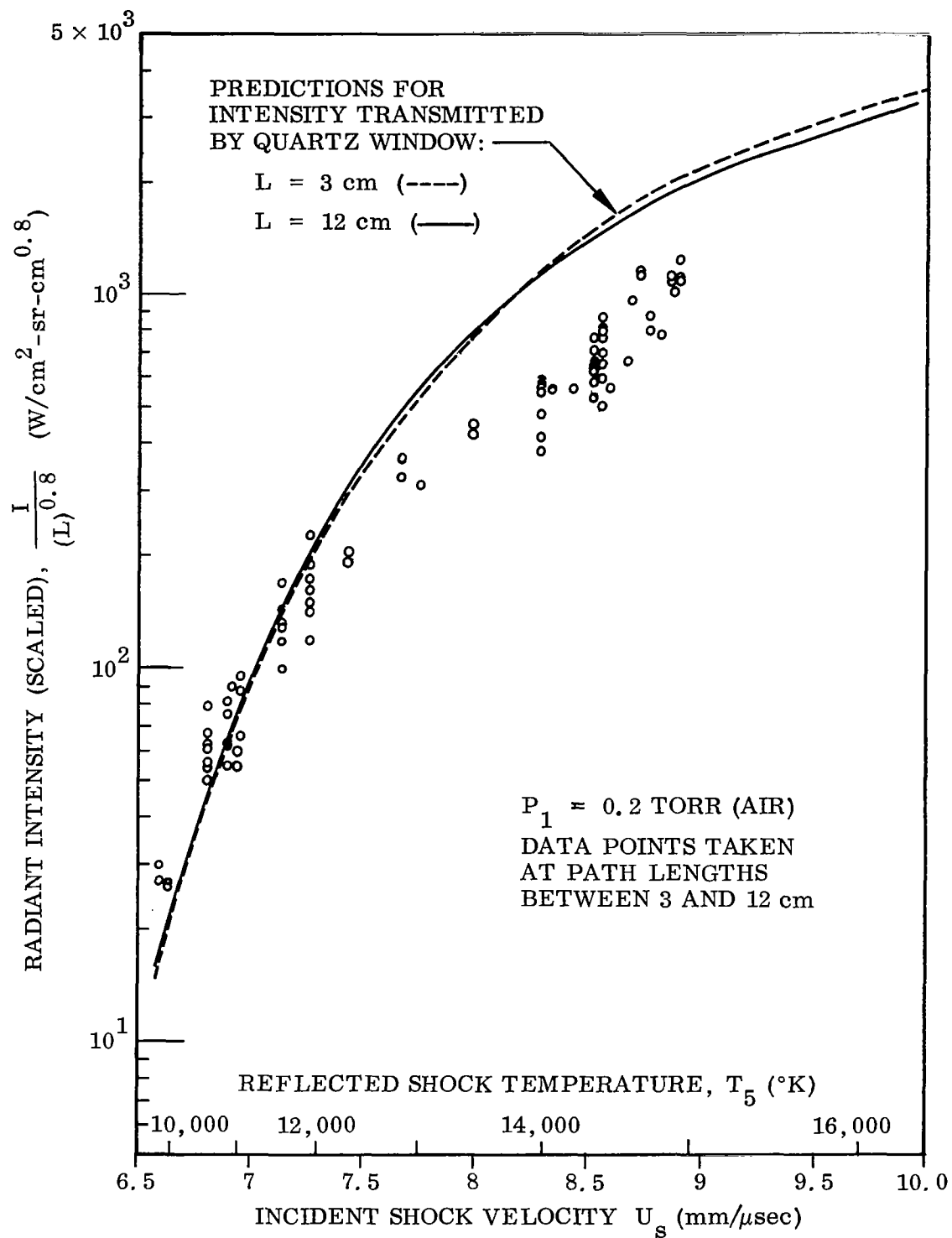


Fig. A2 Experimental Results and Theoretical Predictions for the Radiant Intensity Transmitted by a Quartz Window.

TABLE A1

RADIANT INTENSITY PREDICTIONS AT CONDITIONS IN THE REFLECTED SHOCK REGION

Conditions	Path δ , cm	ALL INTENSITIES HAVE UNITS OF W/CM^2-SR						
		Line <2000A	Line >2000A	Con- tinuum <2000A	Con- tinuum >2000A	Neg. Ion	Molecular Band	Total
(6.6 mm/ μ sec)	1	10.1	7.79	8.21	2.29	3.71	1.74	33.9
9,762 K	3	15.8	17.0	13.6	6.81	11.1	5.22	69.6
2.184 atm	5	19.4	24.4	16.5	11.3	18.5	8.70	98.8
	8	23.4	33.4	19.1	18.0	29.7	13.9	137
	12	27.8	43.6	21.0	26.8	44.5	20.9	185
(6.8 mm/ μ sec)	1	33.3	20.0	25.2	8.09	8.75	2.04	97.4
10,490 K	3	51.3	44.0	40.1	24.0	26.2	6.12	192
2.380 atm	5	62.1	62.9	47.6	39.6	43.8	10.2	266
	8	73.7	85.6	53.9	62.8	70.0	16.3	362
	12	88.7	112	58.4	93.1	105	24.5	481
(7.2 mm/ μ sec)	1	172	73.9	120	46.1	29.0	2.26	443
11,710 K	3	248	163	179	135	86.8	6.77	819
2.791 atm	5	304	229	207	220	145	11.3	1,120
	8	299	309	230	344	232	18.1	1,430
	12	348	397	248	504	348	27.1	1,870
(7.8 mm/ μ sec)	1	746	237	484	215	85.4	2.00	1,770
13,070 K	3	799	507	694	611	256	6.00	2,870
3.437 atm	5	961	691	789	983	427	10.0	3,860
	8	1,120	902	874	1,510	682	16.0	5,110
	12	1,290	1,110	961	2,170	1,020	24.0	6,590
(8.4 mm/ μ sec)	1	1,300	849	1,210	568	167	1.30	4,090
14,160 K	3	1,890	995	1,700	1,570	502	4.50	6,650
4.083 atm	5	2,190	1,300	1,930	2,490	835	7.50	8,740
	8	2,440	1,600	2,150	3,750	1,330	12.0	11,300
	12	2,780	1,800	2,410	5,280	2,000	18.0	14,300
(9.0 mm/ μ sec)	1	3,110	770	2,320	1,070	246	-	7,520
15,080 K	3	3,390	1,470	3,240	2,910	738	-	11,800
4.601 atm	5	3,910	1,740	3,690	4,530	1,230	-	15,100
	8	4,220	2,070	4,160	6,690	1,970	-	19,100
	12	4,820	2,330	4,720	9,220	2,950	-	24,000
(9.6 mm/ μ sec)	1	4,820	1,010	3,710	1,590	291	-	11,400
15,870 K	3	5,150	1,840	5,220	4,240	872	-	17,300
4.889 atm	5	5,550	2,110	5,970	6,530	1,450	-	21,600
	8	6,220	2,420	6,780	9,510	2,330	-	27,300
	12	6,910	2,630	7,710	12,900	3,490	-	33,700
(10.2 mm/ μ sec)	1	7,230	1,280	5,830	2,300	341	-	17,000
16,700 K	3	7,500	2,090	8,250	6,030	1,030	-	24,900
5.374	5	8,060	2,460	9,490	9,160	1,710	-	30,900
	8	8,940	2,710	10,800	13,200	2,730	-	38,300
	12	9,810	2,870	12,300	17,700	4,090	-	46,800

TABLE A2

CALCULATED THERMODYNAMIC STATES OF THE REFLECTED SHOCK REGION

(P₁ = 0.2 Torr, T₁ = 294 °K, Gas 79% N₂, 21% O₂ by pressure)

U _S mm/ μsec	T ₅ °K	P ₅ atm	ρ ₅ gm/cc	H ₅ cal/gm	NUMBER DENSITIES IN PARTICLES/(CM) ³								
					e	N	O	N ⁺	O ⁺	N ₂	O ₂	N ⁻	O ⁻
6.6	9,762	2.184	3.917 ⁻⁵	1.107 ⁺⁴	2.07 ⁺¹⁶	1.25 ⁺¹⁸	3.42 ⁺¹⁷	1.74 ⁺¹⁶	3.24 ⁺¹⁵	1.43 ⁺¹⁶	7.24 ⁺¹²	1.30 ⁺¹²	5.41 ⁺¹²
6.8	10,490	2.381	3.912 ⁻⁵	1.181 ⁺⁴	3.86 ⁺¹⁶	1.25 ⁺¹⁸	3.38 ⁺¹⁷	3.28 ⁺¹⁶	5.78 ⁺¹⁵	6.31 ⁺¹⁵	5.12 ⁺¹²	2.34 ⁺¹²	7.90 ⁺¹²
7.2	11,710	2.791	3.976 ⁻⁵	1.331 ⁺⁴	9.24 ⁺¹⁶	1.24 ⁺¹⁸	3.37 ⁺¹⁷	7.93 ⁺¹⁶	1.33 ⁺¹⁶	1.99 ⁺¹⁵	3.25 ⁺¹²	5.11 ⁺¹²	1.32 ⁺¹³
7.8	13,070	3.437	4.144 ⁻⁵	1.566 ⁺⁴	2.02 ⁺¹⁷	1.20 ⁺¹⁸	3.36 ⁺¹⁷	1.73 ⁺¹⁷	2.89 ⁺¹⁶	6.71 ⁺¹⁴	2.17 ⁺¹²	9.84 ⁺¹²	2.06 ⁺¹³
8.4	14,160	4.083	4.275 ⁻⁵	1.816 ⁺⁴	3.34 ⁺¹⁷	1.13 ⁺¹⁸	3.28 ⁺¹⁷	2.86 ⁺¹⁷	4.86 ⁺¹⁶	3.00 ⁺¹⁴	1.57 ⁺¹²	1.41 ⁺¹³	2.64 ⁺¹³
9.0	15,080	4.601	4.248 ⁻⁵	2.078 ⁺⁴	4.69 ⁺¹⁷	1.01 ⁺¹⁸	3.04 ⁺¹⁷	3.99 ⁺¹⁷	7.03 ⁺¹⁶	1.44 ⁺¹⁴	1.10 ⁺¹²	1.65 ⁺¹³	2.87 ⁺¹³
9.6	15,870	4.889	4.028 ⁻⁵	2.350 ⁺⁴	5.83 ⁺¹⁷	8.43 ⁺¹⁷	2.64 ⁺¹⁷	4.92 ⁺¹⁷	9.07 ⁺¹⁶	6.78 ⁺¹³	7.03 ⁺¹¹	1.61 ⁺¹³	2.69 ⁺¹³
10.2	16,700	5.374	3.947 ⁻⁵	2.646 ⁺⁴	7.18 ⁺¹⁷	7.08 ⁺¹⁷	2.32 ⁺¹⁷	6.02 ⁺¹⁷	1.16 ⁺¹⁷	3.27 ⁺¹³	4.57 ⁺¹¹	1.56 ⁺¹³	2.52 ⁺¹³
10.8	17,610	6.037	3.946 ⁻⁵	2.967 ⁺⁴	8.74 ⁺¹⁷	5.83 ⁺¹⁷	1.99 ⁺¹⁷	7.26 ⁺¹⁷	1.48 ⁺¹⁷	1.53 ⁺¹³	2.86 ⁺¹¹	1.46 ⁺¹³	2.30 ⁺¹³

REFERENCES

1. Wood, A. D., Hoshizaki, H., Andrews, J. C., and Wilson, K. H., "Measurements of the Total Radiant Intensity of Air," AIAA J., Vol. 7, No. 1, 1969, pp. 130-139.
2. Sawyer, R. A., Experimental Spectroscopy, Prentice-Hall, New York, 1951.
3. Harrison, G. R., Lord, R. C., and Loofbourow, J. R., Practical Spectroscopy, Prentice-Hall, Englewood Cliffs, N. J., 1948.
4. Wurster, W. H., "High-speed Shutter for Spectrographs," Rev. Sci. Inst. Vol. 28, No. 12, 1957, pp. 1093-1094.
5. Milne, G. G., and Eyer, J. A., "Problems of Photographic Spectrophotometry of Short Duration Light Pulses: Granularity, Reciprocity Failure, and Latent Image Stability," DASA Report 1332, Aug. 1962.
6. Zel'dovich, Ya. B., and Raizer, Yu. B., (Edited by Hayes, W. D., and Probstein, R. F.), Physics of Shock Waves and High-temperature Hydrodynamic Phenomena (Vol. I), Academic Press, New York, 1966, Chap. III.
7. Wiese, W. L., Smith, M. W., and Glennon, B. M., "Atomic Transition Probabilities, Vol. I, Hydrogen Through Neon," National Bureau of Standards Report No. NSRDS-NBS4, May 1966.
8. Page, W. A., Compton, D. A., Borucki, W. J., Ciffone, D. L., and Cooper, D. M., "Radiative Transfer in Inviscid Nonadiabatic Stagnation-region Shock Layers," AIAA Paper 68-784, June 1968, AIAA 3rd Thermophysics Conference, Los Angeles, Calif.
9. Wilson, K. H., and Nicolet, W. E., "Spectral Absorption Coefficients of Carbon, Nitrogen, and Oxygen Atoms," J. Quant. Spectros. Radiat. Transfer, Vol. 7, 1967, pp. 891-941.

10. Griem, H. R., Plasma Spectroscopy, McGraw-Hill, San Francisco, 1964.
11. Morris, J. C., Krey, R. U., and Garrison, R. L., "Radiation Studies of Arc Heated Nitrogen, Oxygen, and Argon Plasmas," ARL 68-0103, May 1968, Aerospace Research Laboratories, Office of Aerospace Research, USAF.
12. Armstrong, B. H., Johnston, R. R., and Kelley, P. S., "Opacity of High Temperature Air," LMSC 8-04-64-2, Nov. 1964, Lockheed Missiles and Space Co., Sunnyvale, Calif. (also Air Force Weapons Laboratory Report AFWL-TR-65-17).
13. Moore, C. E., "A Multiplet Table of Astrophysical Interest (1945 Edition)," NBS Technical Note 36, Nov. 1959.
14. Morris, J. C., Krey, R. U., and Bach, G. R., "The Continuum Radiation of Oxygen and Nitrogen for use in Plasma Temperature Determination," J. Quant. Spectros. Radiat. Transfer, Vol. 6, 1966, pp. 727-740.